Coherent structures in a round, spatially evolving, unforced, homogeneous jet at low Reynolds numbers

Ionut Danaila
I.N.E.R.I.S., Parc Tech. Alata, 60550 Verneuil en Halatte and I.R.P.H.E., 12 Av. Général Leclerc, 13003 Marseille, France

Jan Dušek
I.M.F., 2 rue Boussingault, 67000 Strasbourg, France

Fabien Anselmet
I.R.P.H.E., 12 Av. Général Leclerc, 13003 Marseille, France

(Received 13 August 1996; accepted 1 July 1997)

Three–dimensional direct numerical simulations of unforced, incompressible, free, spatially evolving round jets are used to investigate the onset of instability at low diametral Reynolds numbers ($Re \leqslant 500$). Compact, coherent structures are identified by means of iso-surfaces of vorticity and pressure fields and shown to be synonymous with instability modes. Once the inflow velocity profile is fixed, as the Reynolds number increases from 200 to 500, the most amplified unstable mode switches from the helical mode to the axisymmetric one, as expected from the predictions of the viscous linear stability theory analysis and from experimental observations [J. Fluid Mech. **77**, 511 (1976); Prog. Aerosp. Sci. **21**, 159 (1984)] [J. Fluid Mech. **48**, 547 (1971)]. At the upper limit of the investigated range of Reynolds numbers, the present simulations are consistent with the widely accepted scenario of the space time development of the round jet instability. This scenario is analyzed in detail. The appearance of pairs of axially counter-rotating vortex filaments is found (for the first time, to our knowledge, in unforced, spatial numerical simulations) to characterize the destabilization of initial axisymmetric vortical structures. The spatial evolution of these structures is investigated and their role in vortex rings reconnection is evidenced. For lower Reynolds numbers, a superposition of symmetry-breaking (helical) modes is shown to characterize the instability of the round jet. The Fourier decomposition of the fluctuating flow field allows the extraction of the helical modes and the identification of the flow patterns resulting from their interactions. The attractor is shown to be a limit torus very close to the onset of the instability. © *1997 American Institute of Physics.* [S1070-6631(97)01911-9]

I. INTRODUCTION

Since Rayleigh introduced stroboscopic illumination (1884) for flow visualizations and analyzed the jet instability problem (1879) (cf. Ref. 1), the multitude of experimental, analytical and numerical studies concerning the free, homogeneous, axisymmetric jet instability have considered two distinct types (modes) of instabilities.

(1) Varicose instability, characterized by axisymmetric modes in which waves travel as a succession of symmetrical swellings and contractions.
(2) Sinuous instability, characterized by helical (spiral) modes in which the waves appear as a rhythmic undulation or twisting of the jet.

At the present time, the onset of one type of instability or another for the naturally evolving jet is not well defined in terms of the Reynolds number range. In the literature, most of the studies deal (because of engineering applications) with high Reynolds number jets (often forced) where the axisymmetric modes are the most amplified. The presence of the helical (symmetry-breaking) modes in the jet flow is reported, at low Reynolds numbers, by both linear stability analysis and experimental studies, but reliable experimental and numerical data are not available for these Reynolds number values.

The main purpose of this paper is to examine the coherent structures dominating the flow at the onset of instability in a naturally evolving axisymmetric jet. We shall focus, primarily, on low diametral Reynolds number jet flows ($Re < 500$), which are of basic theoretical importance for the development of instabilities and for which the available experimental data appear to be incomplete and sometimes contradictory. We examine the selection of the dominating unstable modes — varicose or helical — during the instability development and for different Reynolds numbers. Quantitative tools for their detailed description are provided. The originality of the present simulations is given by the fact that the instability onset is not forced, but it naturally occurs due to the ''numerical noise.''

A. Experimental point of view

The early experimental work indicates that a general agreement on the critical Reynolds number and the evolution with the Reynolds number of the instability in an axisymmetric jet is difficult to obtain. Viilu[2] reports the presence of instability for diametral Reynolds numbers exceeding 10. Reynolds[3] investigated the minimum Reynolds number for instability in an axisymmetric dyed water jet submerged in a water tank. Four different shapes of the flow, defined by ranges of Reynolds number, were reported. For $10 < Re$

<30 the steady state of the jet could be maintained (though with difficulty). For $30<Re<150$ axisymmetric condensations were observed, but further work[4] showed that the axisymmetric condensations were due to the presence of appreciable background disturbances in the experimental apparatus. For $150<Re<300$ sinuous, long wavelength, undulations and a complex breakup occurred. For $Re>300$ the flow was disordered, even near the nozzle.

Becker and Massaro[1] used air jets with a Reynolds number in the range $600<Re<20000$. For the low Reynolds number regime, the observations are less detailed: for the unforced jet at $Re=1690$ the disturbance observed was sinuous and occurred at some distance downstream (5 nozzle diameters); sinuous instability was not observed at Reynolds numbers above 2300.

The experiments of Crow and Champagne[5] showed a continuous evolution of the dyed water jet shape from a sinusoid to a helix, and finally to a train of axisymmetric waves, as the Reynolds number increases from 100 to 1000.

Mollendorf and Gebhart[4] studied buoyant water jets at low Reynolds numbers ($138<Re<537$). For slightly buoyant jets at Reynolds numbers of 250 and 316 the symmetrical disturbances introduced in the flow were seen to damp out, while the asymmetric (helical) disturbances were highly destabilizing. Very small amounts of buoyancy destabilize the flow, but the spiral modes are still the most amplified.

As a consequence of the convectively unstable nature of the incompressible, spatially evolving mixing layer,[6] a free homogeneous jet is expected to be driven by surrounding disturbances, which can explain the existence of few and less conclusive experimental studies at low Reynolds numbers. Nevertheless, the existing studies pointed out two important features of the evolution of the jet flow instability for low Reynolds numbers ($Re<1000$): the Reynolds number is a relevant parameter for the selection of the most amplified mode, and the typical evolution of the jet instability, as the Reynolds number increases, is the continuous shift from the helical mode to the axisymmetric mode.

Experiments show that high Reynolds numbers or forced jets can reduce the influence of external mechanisms on the onset of instability; an abundant literature was constituted in the last 50 years in this field (see Ref. 7 for references). For a large range of Reynolds numbers ($5500<Re<10^6$), the varicose instability was observed and the scenario of the early stages of evolution of the round jet seems to be universal (independent of the Reynolds number): the shear layer originating from the nozzle lip is inviscidly unstable via the Kelvin–Helmholtz primary instability mechanism;[8] the instability waves grow downstream and roll up into coherent vortex rings;[9] the structures merge as they are convected downstream and determine the shear layer spread;[10] streamwise vortex structures develop through a secondary three–dimensional instability of the thin vorticity layer (*braid*) between two neighboring vortex rings.[11]

B. Theoretical point of view

From a theoretical point of view, the axisymmetric jet has two distinct instability length-scales: the initial shear-layer momentum thickness (Θ_0), describing the near field dynamics (near the jet exit) and the jet diameter (D) governing the evolution in the far field (above the end of the potential core). The two corresponding instability modes are the high frequency *shear-layer mode* and the low frequency *jet-column mode* (or *preferred mode*).[8]

Stability characteristics of the round jet flow can be locally described by the linear stability analysis, assuming an undisturbed (base) parallel jet flow, infinitely extended in the up and downstream directions. As in a real jet the shape of the local mean velocity profile evolves along the downstream direction, different types of base velocity profiles are analyzed. The inviscid linear analysis of Batchelor and Gill[12] demonstrated the unstable character of the *top-hat* velocity profile (representing the flow close to the jet exit) with respect to axisymmetric as well as helical modes for all values of the stream-wise wavenumber.

Mattingly and Chang[13] considered the inviscid instability of the experimental velocity profiles for a Reynolds number of 300 and showed that the axisymmetric mode dominated close to the jet exit, whereas downstream of three nozzle diameters the helical mode achieved the maximum amplification.

The inviscid linear analysis of Plaschko[14] allows for slightly diverging flows. It indicates that for large values of the Strouhal number of the perturbation (i.e., near the nozzle lip) the axisymmetric instabilities are more amplified than their spiral counterparts; at a lower Strouhal number (occurring at the end of the potential core) the first helical mode is more unstable than the axisymmetric one.

Michalke[15] used a family of tanh-velocity profiles to evaluate the local instability of the jet flow to the end of the potential core. For the inviscid linear stability analysis, the relevant jet parameter is the local ratio between the jet half-width (R) and the momentum thickness (Θ). The growth rate of the first helical disturbances ($m=1$) for $R/\Theta>25$ is not much different to that of axisymmetric disturbances ($m=0$). For $R/\Theta=10$ the growth rate for $m=0$ is larger than that for $m=1$, while the inverse is true for $R/\Theta=5$. In the real jet, the jet parameter R/Θ decreases in the downstream direction and consequently, the initial region of the jet is equally unstable to both $m=1$ and $m=0$ modes, while at the end of the potential core $m=1$ is the most amplified mode.

The linear stability analysis was extended to include viscous effects by Morris.[16] Jet velocity profiles characterizing several stages of development of the round jet were examined. Above a Reynolds number of 1000 the influence of viscosity on the growth rate was obviously small for a fixed jet parameter (R/Θ). For a tanh-velocity profile, representative of the region towards the end of the potential core, the Reynolds number is the parameter selecting the most amplified unstable mode in the range $100<Re<500$. For $Re=500$, the maximum growth rate of $m=1$ is slightly larger than that of $m=0$ and with decreasing Re, the axisymmetric mode becomes significantly less unstable than the helical one.

The viscous, linear stability analysis was applied by Mollendorf and Gebhart[4] for the round jet, using a boundary-layer base flow (characteristic of the far field). It was found that the first helical mode was amplified over shorter dis-

tances as the frequency and Reynolds number increased. The axisymmetric mode was found to be unconditionally stable.

The local parallel theory describes well the initial development of the instability in high Reynolds number jets, but its applicability in analyzing real jet flows is limited to short distances in the stream-wise direction. For the unperturbed jet ($Re=42000$), Cohen and Wygnanski[17] found good agreement between the inviscid linear stability results and the experimental data for a narrow zone near the nozzle ($0.125<z/D<0.25$), where the variation of the local momentum thickness was negligible. They also underlined the main drawback of the local linear stability theory which is unable to account for the spread of the shear layer; in reality, Θ increases downstream and the most amplified instability waves shift toward lower and lower frequencies. Indeed, it has been shown[18] that the unstable wave is sensitive only to mean flow features extending over length-scales exceeding its wavelength. In jets, this wavelength is typically of the order of the diameter even close to the nozzle (≈ 0.6 for $R/\Theta=50$ and $Re=500$ in the parallel analysis of the initial mixing region profile of Ref. 16). Consequently, one could expect the entire evolution of the mean velocity profiles in the initial zone corresponding to the first wavelengths to be significant for the development of the unstable mode, and not only the inflow velocity profile, as usually assumed.

C. Numerical point of view

Direct numerical simulations have proven very effective in elucidating features of the primary and secondary instabilities of the axisymmetric jet. The numerical ''experiments'' eliminate uncontrollable disturbances, usually occurring in the laboratory experimental devices, but they bring the problem of boundary conditions. Inflow and outflow boundary conditions must be as *transparent* as possible, meaning that unphysical reflections at the boundaries should be minimal. Partly to elude this difficulty, partly to reduce the domain size and to zoom on a single coherent structure the great majority of the simulations use the so-called ''temporal'' model, which assumes the flow to be spatially periodic in the downstream direction.

Temporally evolving three-dimensional calculations, using vortex filaments,[19] spectral[20,21] finite-differences[22] or combined spectral-finite-differences techniques,[23] are helpful in understanding the dynamics of the vorticity flow field and the evolution of coherent structures. Meanwhile, it should be emphasized that there is no exact transformation between temporally and spatially evolving shear flows.[24] Consequently, temporal simulations are depleted of any *spatial* information (as flow spreading) and offer only a qualitative description of the evolution of vortex structures.

However, laboratory flows evolve both in space and in time, and a more realistic simulation must be based on the ''spatial'' model. For non parallel flows, the parallel or weakly parallel theory may be unable to distinguish really unstable global modes,[18] the stream-wise coupling being essential for the determination of their instability.[6] Numerical simulations for forced[25] or unforced[26,27] spatially developing axisymmetric mixing layers assume that the essential jet dynamics is inviscid and consequently, simulate high Reynolds numbers ($10^3 \leqslant Re \leqslant 10^6$) flows. Recent development of the large eddy simulation techniques allowed fully 3D, spatial simulations of free forced jets, for relatively high Reynolds numbers ($Re \approx 20000$),[28,29] but, surprisingly, the extent of literature on detailed numerical simulations of spatially, unforced 3D jet flows, for low Reynolds numbers is very limited.

D. Paper organization

The paper is organized as follows. The main features of the numerical implementation and data concerning the influence of the numerical discretization and boundary conditions on the accuracy of the solution will be presented in Section II. The techniques used for the coherent structures visualizations are briefly discussed in Section III. In Section IV we will describe the numerical results for a Reynolds number of 500, when the varicose mode dominates the instability onset. Our simulations follow the instability development until a chaotic asymptotic state is reached. A behavior very similar to that reported from experiments and other simulations at significantly higher Reynolds numbers is found. The experimentally and numerically reported coherent structures described at the end of subsection I A are obtained and compared with previous simulations in periodic configurations. In Section V we will focus on the primary instability investigations. At low Reynolds numbers (at $Re=300$ and below) the observed characteristics of the instability confirm that the helical modes are the most amplified. A method for the splitting of the fluctuating flow field in helical modes and a description of the dynamic characteristics for Reynolds numbers near the onset of unsteadiness are given. Finally, in Section VI, we will draw some conclusions and possibilities for future investigations.

II. NUMERICAL IMPLEMENTATION

Direct numerical simulations of three-dimensional, spatially evolving jets at low Reynolds numbers, are performed using the NEKTON code based on a spectral element method. The NEKTON code was successfully used in various studies concerning flow instabilities.[30–32] A detailed description of the numerical procedures allowed by the NEKTON code (domain design, computation of the time-dependent solution and data post-processing) is given by Neitzel *et al.*[32]

The code allows fully 3D simulations by filling the computational domain with spectral elements in all three spatial directions. NEKTON uses Langrangian interpolation on a Gauss–Lobatto–Legendre mesh. In the predictor step, the velocity field is calculated; the pressure and convective terms are treated explicitly (a third order Adams–Bashforth multi-step scheme is provided). The diffusion terms are treated implicitly by using a third-order backward differentiation multi-step scheme. The corrector step provides the pressure correction as the solution of a Poisson equation and the velocity field correction as that of a Helmholtz equation. Both linear systems are solved by a pre-conditioned conjugate gradient method.

The most important advantage of the spectral element discretization is its local (within one element) spectral accuracy that can be non uniformly distributed throughout the computational domain in order to capture very disparate length scales existing in different regions. It has to be remarked that this flexibility brings about a drawback in the form of discontinuities of the velocity field derivatives at element interfaces. This might be a nuisance if a specific local detail of the flow needs to be known. For the purpose of instability investigation it appeared, however, that the impact of these discontinuities on the instability investigation is quite moderate and can fairly easily be quantified.[33] A similar three-dimensional discretization has recently been used with success to simulate the dynamics of the wake of a finite cylinder:[34] the impact of local inaccuracies on the global behavior was shown to result barely in shifting the critical Reynolds number downward and the frequencies upward.

A. Selection of physical parameters of the spatial simulation. The inflow velocity profile

The simulation of a spatially evolving jet approaches most closely an experimental setup. Our geometrical configuration simulates an unconfined round jet issuing from a circular orifice of diameter $D=2R_0$ in a solid (no slip) wall. As mentioned in Section I B, the diameter of the orifice fixes the characteristic length scale of the simulation. The velocity scale is given by the maximum of the inflow stream-wise velocity $(V_{z0})_{max}$. The ratio $t_0=D/(V_{z0})_{max}$ yields the used time scale. In what follows, all the quantities are non dimensionalized using these characteristic scales. The resulting Reynolds number is defined as $Re=(V_{z0})_{max}D/\nu$.

An important effort has been made to optimize the discretization parameters in order to capture all possible states of the jet flow in the Reynolds number range of $10\leqslant Re \leqslant 500$. The mesh is shown in Fig. 1. It has 65 three-dimensional spectral elements, covering an axisymmetric computational domain of radial size $D_{max}=10.66$ and longitudinal length $L_z=20$. Note that the slowly diverging distribution of the 3D spectral elements in the downstream direction was iteratively obtained in order to follow the space evolution of the jet mixing layer.

In the absence of reliable experimental data, the choice of the inflow profile is not straightforward. Two types of velocity profiles were used as inflow boundary condition: a *top–hat* velocity profile $[V_{z0}(r)=1, r<R_0$ and $V_{z0}(r)=0, R_0<r]$ and the largely used[20,21] hyperbolic tangent (tanh) profile (profile 1 from Ref. 35),

$$V_{z0}(r)=0.5\{1+\tanh[0.5R_0/\Theta_0(1-r/R_0)]\}, \tag{1}$$

where $\Theta_0=\int_0^\infty V_{z0}(r)(1-V_{z0}(r))dr$ is the initial momentum thickness. We considered that a jet parameter (R_0/Θ_0) larger than 20 is necessary for this study. Indeed, for such a ratio, the linear stability theory shows that, though the maximum inviscid amplification rates are similar for the first helical mode $(m=1)$ and the varicose mode $(m=0)$, the Reynolds number is the parameter selecting the most amplified unstable mode, when it varies between 100 and 1000. The ratio of $R_0/\Theta_0\approx 20$ is already obtained with 7 collocation points. To resolve the initial shear layer the spatial discretization has to accommodate a global length scale ratio L_z/Θ_0 of almost one thousand. The spectral element spatial discretization implemented in the NEKTON code is particularly efficient for this purpose (note that a similar ratio would require a prohibitively large mesh if a homogeneous finite difference discretization was to be used).

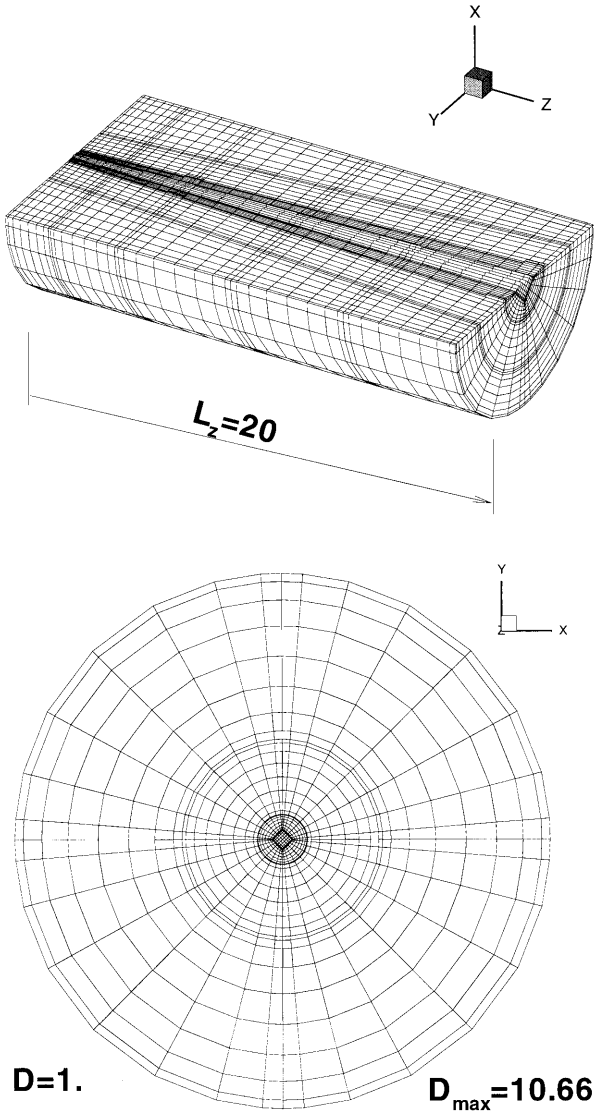

FIG. 1. Spectral elemental mesh obtained with 9 collocation points in each spatial direction. The computational domain has 65 spectral elements (*grid 1*).

B. Numerical accuracy and mesh optimization. Physical meaning of the unforced jet simulation

Preliminary computations[33,34] indicated that, of the three formulations available in NEKTON, the ''split'' (fractional step method) formulation provides accuracy equal to other formulations with a substantial reduction in CPU time (see also Ref. 32). The overall time accuracy of this semi-implicit formulation is of $\mathcal{O}(\Delta t)$ only. However, the local refinement existing in the nozzle and a rather high Reynolds number result in a very restrictive CFL criterion, because the implicit treatment is based on the inversion of the Laplacian operator

TABLE I. (a) Influence of the discretization accuracy on the primary instability characteristics: the critical Reynolds number and the critical Strouhal number. For the reference simulation (grid 1, $L_z=20$, *top-hat* inflow velocity profile, Norder=7) $Re_{cr}=220$, $St_{cr}=0.169$. (b) Influence of the Norder parameter on the *preferred* Strouhal number for $Re=500$.

(a)

Type of test	Variation of Re_{cr} (%)	Variation of St_{cr} (%)
Influence of the domain length		
$L_z=20\rightarrow L_z=15$	1.75	0.59
Influence of the inflow velocity profile		
$top-hat\rightarrow tanh(R/\Theta_0=23.6)$	3.20	0
Influence of the azimuthal resolution		
grid 1→grid 2	1.52	0.29
Influence of the jet mixing layer resolution		
grid 1→grid 3		
(**tanh* velocity profile)	4.41	1.77
Influence of the Norder parameter		
Norder=7→Norder=9	30.90	23.10

(b)

	grid 1, Norder=7	grid 1, Norder=9	grid 1, Norder=11
Nodes	22 295	47 385	86 515
St_D	0.405	0.310	0.387

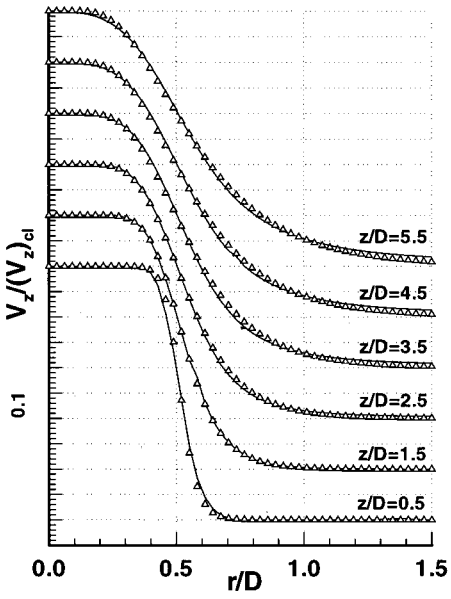

FIG. 2. Unperturbed base velocity profiles for $Re=500$ (solid lines). The symbols represent the theoretical tanh-velocity profile [eq. (2)].

in the Navier–Stokes equations. For example, at $Re=500$ and with 9 collocation points, 250 time steps correspond to the shortest time scale in the simulation, which makes higher order time-stepping pointless.

Our three-dimensional calculations are performed in Cartesian coordinates in a cylindrical computational domain. The azimuthal breakup of the domain into spectral elements makes that the space discretization is not strictly axisymmetric. The effect of this inaccuracy has been tested by increasing the number of elements in the azimuthal direction by a factor of two (8 instead of 4). The test consisted in monitoring the changes of the parameters of the instability observed at $Re=225$. No appreciable differences were stated (see Table Ia and Section V).

The parameters characterizing the domain discretization are its decomposition into spectral elements and the choice of the number of collocation points per spatial direction inside an element (Norder parameter). As far as the size of the elements and their distribution is concerned, our previous experience with two- and three-dimensional discretizations of this type[33,30,34] showed that a good strategy consists in selecting relatively large elements, respecting the requirement that the resolved structures should not be smaller than the size of the element inside which they are situated. The presence of the jet and its shear layer led to the choice represented in Fig. 1. The relatively large size of the elements yields some (limited in three-dimensions) overhead for choosing a high enough spectral resolution inside the elements. We tested whether the number of collocation points is adequate to resolve such a shear layer by computing the steady velocity profiles of the unperturbed unstable flow giving rise to the unsteadiness. This is quite easy because only a short simulation is necessary for eliminating the numerical transients. We ran simulations at Reynolds numbers $Re=200$, 300 and 500, with 7, 8 and 9 collocation points per spatial direction starting from a steady axisymmetric (within the numerical accuracy discussed above) flow at $Re=200$. The most unfavorable case with the strongest transients and earliest instability onset corresponds to $Re=500$. At $t=20$ the instability (here of the Kelvin–Helmholtz type - see Section IV) only leaves the linear regime and the mean flow can be considered as a reasonable approximation of the unperturbed (base) flow. The velocity profiles have thus been obtained as mean values in the non dimensional time interval $7<t<15$ (the numerical transients decay at about $t=6$). These profiles have, indeed the expected character (plotted in Fig. 2 at $Re=500$ for 9 collocation points) which is very well reproduced by the formula (profile 2 from Ref. 35)

$$V_z(r)/(V_z)_{cl}=0.5\{1+\tanh[0.25R/\Theta(R/r-r/R)]\}, \quad (2)$$

where R and $(V_z)_{cl}$ are, respectively, the local half-width and the centerline stream-wise velocity, and the local momentum thickness Θ is defined in the usual way:

$$\Theta=\int_0^\infty V_z(r)/(V_z)_{cl}(1-V_z(r)/(V_z)_{cl})dr. \quad (3)$$

As can be seen from Fig. 2 the shear layer is very rapidly dissipated at this Reynolds number. For high Reynolds numbers, the variation of the local jet parameter R/Θ is usually simply expressed as (Refs. 35, 14): $\Theta/R=0.06(z/D)+0.04$. The coefficients of this equation may depend on initial conditions at the nozzle (such as Θ_0) but are independent of the jet exit Reynolds number. In our simulations, with a fixed initial velocity profile (the same Θ_0), we observed that for a varying exit Reynolds number, different downstream evolutions of the local jet parameters are obtained (Fig. 3). Note that for $z/D>0.5$ this variation is within the range $5<R/\Theta<12$ reported by linear stability analysis[35] to be ''sensitive'' for the selection of the most amplified unstable mode ($R/\Theta=5$: $m=1$ is the most amplified, $R/\Theta\approx12$: $m=1$ and m

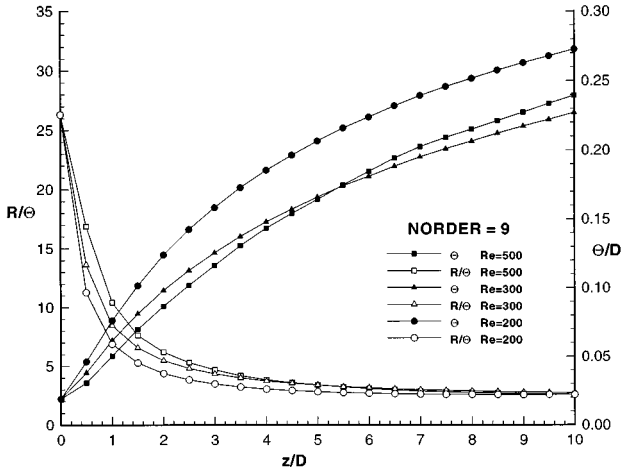

FIG. 3. Stream-wise variation of local jet parameters: local momentum thickness (Θ) and ratio between the local half-width and the local momentum thickness (R/Θ) for different Reynolds numbers and the same numerical discretization (Norder=9).

$=0$ are equally amplified). In addition, the local Reynolds number $Re_l=(V_z)_{cl}(2R)/\nu$ slightly varies along the axis, compared to the inflow Reynolds number (maximum 15% of variation). Consequently, we expect, from the predictions of the viscous stability analysis,[16] that in the considered range, the exit Reynolds number is an important parameter in the selection of the most unstable mode.

We also checked how for a given Reynolds number the profiles vary with increasing discretization accuracy. Although, at the inflow boundary with a *top-hat* velocity profile, the obtained R_0/Θ_0 ratio varied quite considerably (from 20 with 7 collocation points to 26.5 with 9 points and 40 with 11 points), as close as $z=0.5D$ downstream of the nozzle, the $(R/\Theta)(z)$ curves become superimposed. As $0.5D$ corresponds to less than one wavelength (about $0.8D$ — see Fig. 8) of the Kelvin Helmholtz instability evidenced at $Re=500$, the instability is only weakly sensitive to this extremely local difference (see Ref. 18). Indeed, when the *top-hat* profile was replaced by a hyperbolic tangent one [eq. (1)] with $R_0/\Theta_0=23.6$, no appreciable difference in the dynamics of the simulated flow resulted. This explains why a qualitatively very similar behavior to that described in Section IV (9 collocation points used) could be obtained with only 7 collocation points.

The ultimate test of the discretization accuracy is the sensitivity of the instationarity threshold and of the critical frequency to the mesh improvements. All mentioned discretization parameters have been tested on this basis. The results for different test cases are presented in Table Ia. The corresponding radial and azimuthal distribution of spectral elements is presented in Fig. 4.

As far as the sensitivity of the flow to the mesh refinement in the close neighborhood of the nozzle is concerned, it appears that its influence on the critical frequency is moderate. In contrast, the threshold of the instability onset increases quite considerably if the resolution is increased. To understand that, we investigated how the flow field varies if the spatial resolution is improved. We found that the mesh

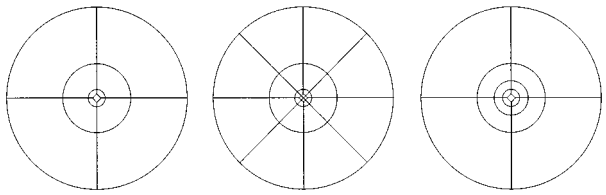

FIG. 4. Radial and azimuthal distribution of spectral elements at the inflow section for the tested grids. From left to right: *grid 1, grid 2, grid 3.*

refinement results in appreciable variations of the flow field only very close ($z<1.5$ D) to the nozzle. If this zone is excluded the mean square variation of the velocity field in the whole computational domain was found to be less than 1% when the resolution was improved from 7 to 11 collocation points. We concluded that the instability in our simulation is triggered by numerical noise in this zone close to the nozzle. This numerical noise does not result from rounding errors and does not introduce any artificial randomness. The instability is forced by the discontinuities of derivatives at spectral element interfaces, which have been recognized[33,34] to tend to force numerically simulated hydrodynamic instabilities in wakes. (In the present case they introduce an artificial recirculation in a very confined neighborhood of the inflow.) This situation is much the same as in experiments, where the onset of instationarity depends on the level of experimental noise. Indeed, it has been recognized[6] that cold jets are convectively unstable and act essentially as noise amplifiers. The critical Reynolds number has thus not much sense if we do not focus on the problem of how the instability is triggered.

The mechanisms of instability generation in experimental devices are of various origins[7] and generate a large scatter ($>50\%$) in the measured parameters such as the *preferred* Strouhal number. The fact that, in our simulations, the Norder parameter yields a varying numerical excitation has been verified for the simulation at $Re=500$. The same scenario of the flow evolution (see Section IV) is found for Norder=7, 9 and 11. The *preferred* Strouhal number varies by, at most, 22%, and remains within the experimentally reported range of variation (see Table Ib). Note that this variation is not monotonic as a function of the Norder parameter, suggesting that it results from local numerical perturbations rather than from the increase of the overall accuracy.

Purely hydrodynamic origins might be investigated numerically, but the fact that the zone of the instability generation is confined in the shear layer close to the nozzle shows that resolving such details represents a further qualitative step going beyond the scope of this paper. As a result, the simulations presented in this paper have to be considered as representing with about 1–3% accuracy the space–time evolution of a jet in a domain extending roughly from 1.5 D to 20 D downstream of the inflow. The instability is generated by a numerical noise of a controlled level (by the Norder parameter) which allows the investigation of a single parameter influence — the Reynolds number — on the unstable mode selection.

C. Boundary conditions and tests

On the circumference of the domain and at its outflow section, the normal pseudo-traction and the tangential viscous stress are set to zero ($-p+1/Re\,\partial_\perp V_\perp=0$, $\partial_\parallel V_\perp+\partial_\perp V_\parallel=0$, where $\perp$ and $\parallel$ denote the normal and tangential directions to the boundary surface). It is assumed that under proper usage, the term $1/Re\,\partial_\perp V_\perp=0$ is negligible at the boundary and therefore the pressure is set to the ambient (zero) pressure at the boundaries. These conditions allow a volume exchange with the outside of the domain. This appeared to be very useful not only to simulate properly the outflow of the domain but also to respect the stream-wise momentum conservation (and thus the mass non conservation). Tests have shown that, unless a prohibitively large domain diameter is used, the confinement effect of the usually used slip-wall lateral boundary conditions is non negligible. With these computational domain dimensions and boundary conditions, the flow was found practically insensitive to a further lateral and downstream increase of the simulation domain.

The absence of spurious reflections at the boundaries, which can affect the solution and even trigger global instabilities[36] was verified. The first numerical test verified that the vortex structures leave the computational domain without reflections. Figure 5 shows the establishment of the flow field for a Reynolds number of 200. The calculation starts from uniform initial conditions. The leading vortex ring travels and expands within the computational domain and finally leaves it properly, without reflections. Without additional forcing, a steady state is obtained at this Reynolds number. In the second numerical test, the computational domain was shortened by the last layer of spectral elements, yielding a domain of $L_z=15$. The highest Reynolds number considered in these simulations was chosen to put to the test the influence of the stream–wise length of the computational domain. The vorticity fields (Fig. 6) are shown to be identical for the two calculations for a long simulation time. For $t=15$ and $t=53.6$ identical structure of the flow can be observed in the two domains; $t=74.3$ corresponds to the onset of chaotic regime in both domains; for $t=94.5$, fairly developed large eddies have comparable behavior in both domains. In conclusion, the vorticity fields are identical for the two calculations for a time period equal to 2.5 times the residence time of the vortex structures within the domain considered ($t\approx 75$), corresponding to the onset of an overall vortex break up.

III. FLOW VISUALIZATIONS

Two intuitive indicators of vortices are easily at hand after a numerical simulation: the pressure minimum and the vorticity surfaces. Jeong and Hussain[37] proved that these criteria are often necessary, but not sufficient to detect a vortex core, especially in wall-bounded or turbulent flows. However, the instantaneous vorticity field provides an effective means of free shear flow visualization and coherent structure identification, comparable with more complicated methods when we focus on the transitional region.

In the early stages of the jet evolution (rolling and pairing), coherent structures with obvious regularity in time and space appear, and the vorticity magnitude ($|\omega|$) is sufficient to detect them.[38] On the other hand, details of the next stages of the jet evolution (secondary instability and further) can be obtained only if the cylindrical components of the vorticity (azimuthal ω_θ, radial ω_r and longitudinal ω_z) are visualized.[21]

In the following sections, coherent structures are visualized by means of iso-surfaces of different components of the vorticity. A useful indicator of the choice of the component to be visualized is provided by the time evolution of the root mean square (RMS) of the instantaneous velocity and vorticity components, defined by the operator[21]

$$(E\phi)(t)=\sqrt{\frac{1}{\pi R_{max}^2 L_{max}}\int\int\int \phi^2(r,\theta,z)\,r\,dr\,d\theta\,dz}. \quad (4)$$

It was seen that all velocity and vorticity components are equally important in the flow analysis. We have to take into account that the size and the number of identified vortices depend on the selected threshold of the identifier; we considered an intermediate low level (35% of the maximum absolute value) in most of the following visualizations.

The pressure minimum criterion, successfully used by Grinstein *et al.*[27] to identify vortex rings in the transitional region of an axisymmetric jet, was also tested. The pressure drops below ambient pressure in the core of the ring and rises above ambient pressure between the rings.

IV. HIGH SUPERCRITICAL REYNOLDS NUMBER

For a Reynolds number of 500, the unforced jet flow simulations use as initial conditions the axisymmetric and steady flow field obtained for $Re=200$. The simulation parameters are $L_z=20$, 65 spectral elements, 9 collocation points and a *top-hat* inflow velocity profile.

After a rapid relaxation of the numerical transients, the initially axisymmetric flow is spontaneously destabilized by the ''numerical noise'' and it undergoes a Kelvin–Helmholtz primary instability. The subsequent evolution of the simulated jet flow provides a qualitative assessment of the formation and dynamics of large scale vortical structures described in the widely accepted scenario for high Reynolds numbers. The most important stages of the flow evolution from a linearly unstable mode to the chaotic stage are detailed and compared with previous findings of ''temporal'' simulations in the following subsections.

A. Vortex roll-up

At this Reynolds number, the steady (basic) flow is linearly unstable, the linear mode being axisymmetric of the Kelvin–Helmholtz type. The local basic velocity profiles in the near field can be well approximated (Fig. 2) by a tanh-velocity profile. The initially slight linear growth of the energy content of the radial velocity Ev_r (Fig. 7, upper plot) and the very small level of the stream-wise vorticity $E\omega_z$ (Fig. 7, lower plot) correspond to the roll-up of coherent vortex rings, characteristic of the saturation of the Kelvin–Helmholtz instability. Frames of the early stages of the flow

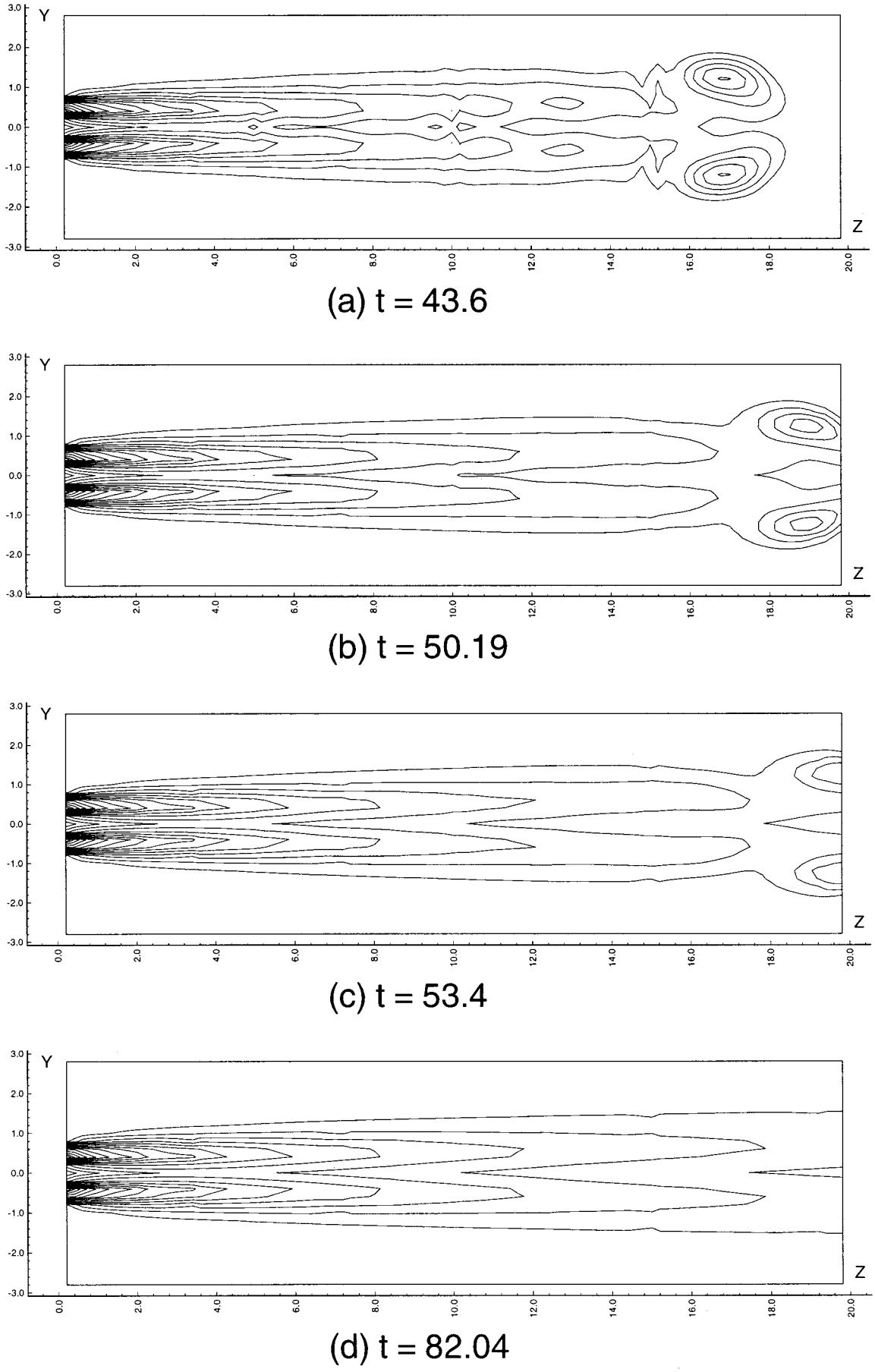

FIG. 5. Exit boundary condition test for $Re = 200$. The calculation starts from uniform initial conditions. Iso-contours of the vorticity ($|\omega|$) are shown.

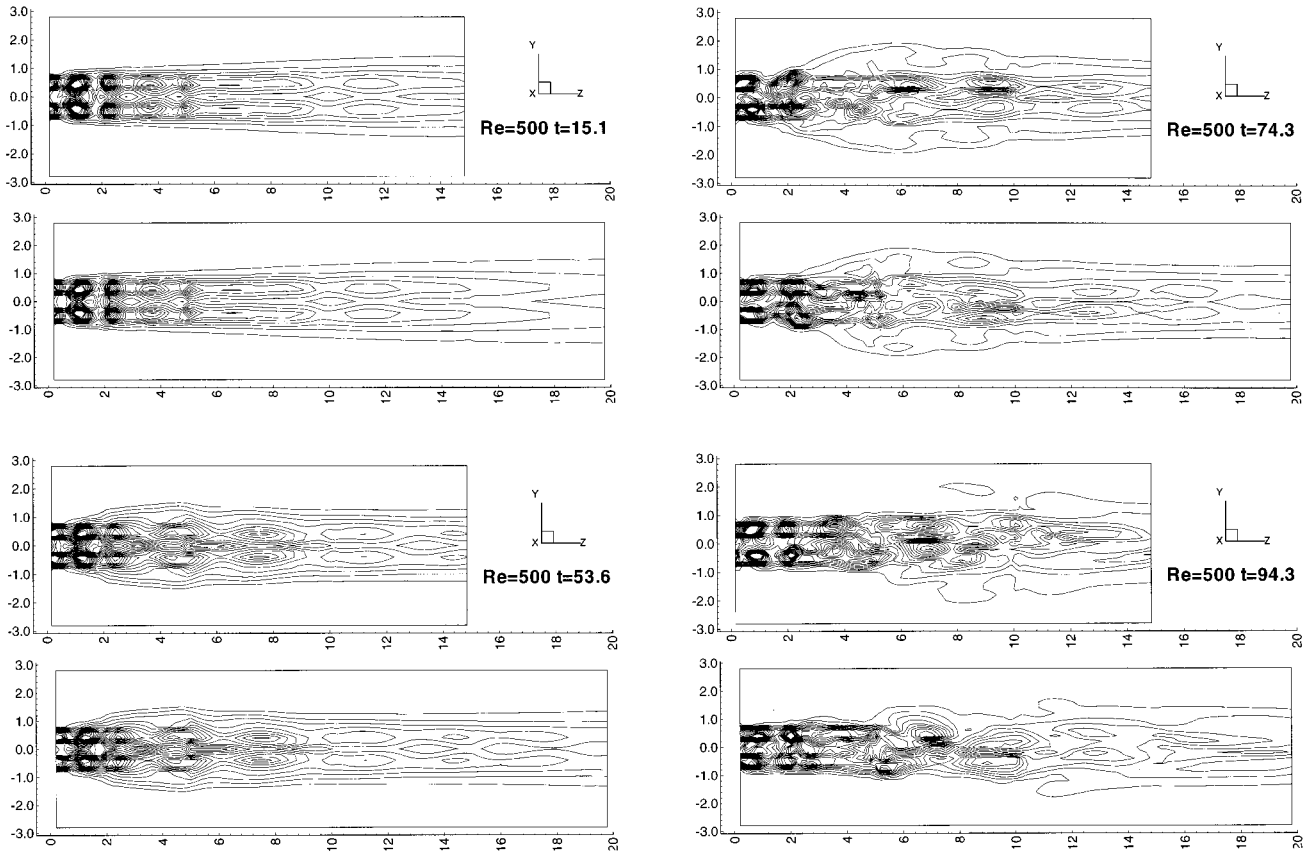

FIG. 6. Test of the influence of the stream-wise size of the computational domain for $Re=500$. The calculation used as an initial condition the steady flow field obtained for $Re=200$.

(Fig. 8) show that rings emerge at an essentially fixed distance from the nozzle edge, $z_{roll}\approx 1.8$. The sequence of the flow evolution, from which the frames in Fig. 8 are extracted, permits us to determine the convection velocity of the vortex rings and their frequency of emergence. The convection velocity is estimated at $V_{zc}\approx 0.48$, very close to the theoretical value of 0.5.[7] A new vortex ring is generated with a regular period of approximately 1.7, which gives a rolling frequency of 0.59. Spectra of the axial velocity signals taken at two different spatial locations on the axis and for the simulation time range $5<t<110$ (Fig. 9a) show a peak very close to this value, at $f_0=0.62$. Figure 10 shows that the vortex pairing begins upstream of the points at which the spectra of Fig. 9a are taken, therefore these spectra are already dominated by the peak corresponding to the half-frequency ($f_0/2$) (see the next subsection). To make a comparison with known theoretical predictions, let us assume that the momentum thickness obtained at $z/D=0.5$ is pertinent (Fig. 3). In view of the fact that the simulation has been found only weakly sensitive to the discretization, we consider the station where the effect of the discretization was already found as negligible. This yields a $\Theta\approx 0.029$ value. The Strouhal number based on this momentum thickness and the jet exit velocity is

$$St_\Theta=\frac{f_0\Theta}{V_{z0}}=0.018,$$

which is in good agreement with the experimental values for the Strouhal number of the most amplified frequency in the jet shear layer, with values scattering from 0.01 to 0.023.[7] The theoretical value for the inviscid shear layer of finite thickness, characterized by a hyperbolic tangent velocity profile, is 0.017.[35]

The Kelvin–Helmholtz instability reaches a level at which non linear effects set on at around $t=20$ (Fig. 7). Vortices with obvious regularity in time and space can be observed in the frames of Fig. 8. At this stage of the flow evolution, the vorticity, essentially constituted by its azimuthal component, concentrates into ring vortices while the braid regions become depleted. The flow field is still axisymmetric; Ev_θ, which evaluates the departure from axisymmetry (Fig. 7), stays two orders of magnitude below Ev_r. It should also be noticed from Fig. 7 that Ev_θ and $E\omega_z$ start to grow before $t=20$, meaning that the secondary instability starts to develop before the saturation of the primary instability.

In Sec. II we mentioned that using a less accurate spatial discretization defined by only 7 collocation points per spatial direction of spectral elements allowed us to have a qualitatively correct picture of the flow behavior. The lower resolution tends to over predict the frequencies. Spectra measured in the same points as in Fig. 9a indicated a higher Kelvin–Helmholtz frequency $f_0=0.806$. The corresponding

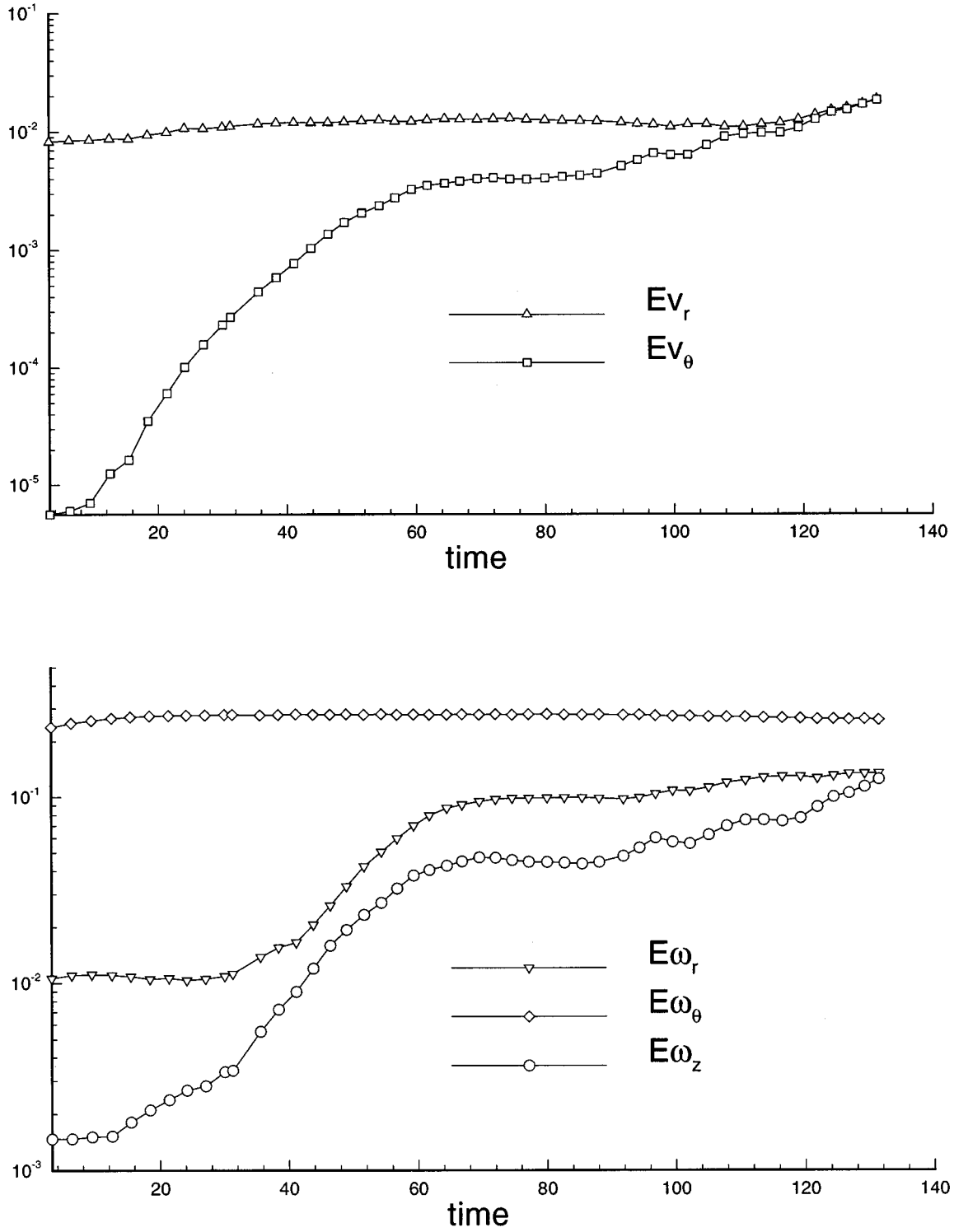

FIG. 7. $Re=500$. Temporal evolution of the energy contents in the velocity and vorticity components. The operator (E) is given by eq. (4).

Strouhal number, based on the momentum thickness at $z/D=0.5$, is then 0.023.

B. Vortex merging

Flow visualization experiments[1,5] have demonstrated that a single vortex–pairing process occurs in the Reynolds number range $3\times10^3<Re\leqslant10^4$. Our simulation for $Re=500$ also shows a single vortex-pairing process. Subsequent flow visualizations, as shown in Fig. 10, allow us to identify the location of the vortex pairing, defined as the place where the two interacting vortices are vertically aligned. In Fig. 10, we can consider that the pairing process is achieved in frame (e) and, consequently, the merging location is $z\approx3.6$.

Frames (a) and (f) are nearly identical, suggesting that the merging occurs with a regular period of approximately

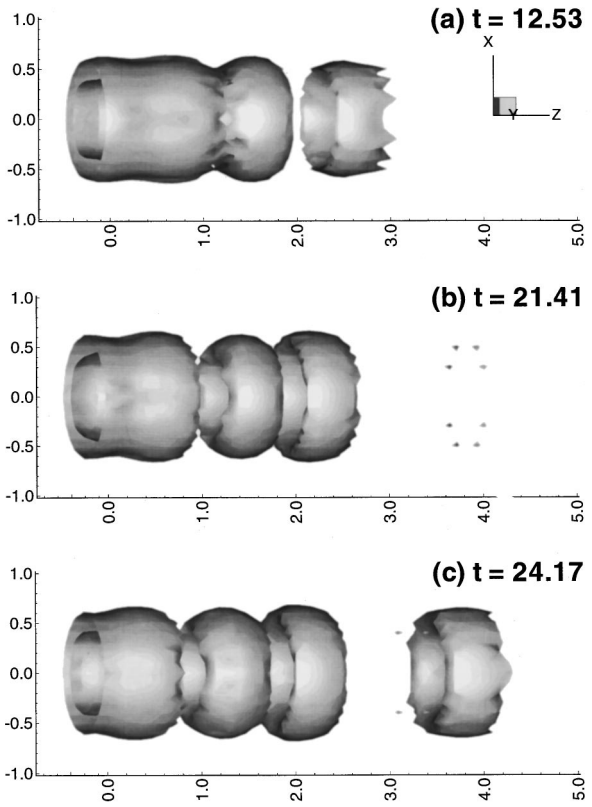

FIG. 8. $Re=500$. Roll-up of the coherent vortex ring phase. Instantaneous surfaces of the constant vorticity magnitude at a threshold of 35% of the maximum value ($|\omega|/|\omega|_{max}=0.35$).

3.02, giving a frequency of 0.33. This frequency is near the highest peak observed in the spectra of Fig. 9a, located at $f_1=f_0/2=0.31$, suggesting that the low frequency peak observed in the spectra corresponds to the frequency of pairings. This finding is in very good agreement with the theoretical and experimental results, showing that vortex pairing is associated with the saturation of the first sub-harmonic $f_0/2$ of the most amplified frequency in the jet shear layer.[8] In terms of the Strouhal number based on the jet diameter $St_D=f_1D/V_{z0}$, the low frequency modulation gives $St_D=0.31$. This is in the range $0.24<St_D<0.5$ in which the *preferred jet mode* is known to lie.[5–7]

We can observe simultaneously the vortical structures before and after merging. The downstream vortex ring grows by viscous diffusion and entrains the smaller upstream ring by vortex induction (Fig. 10). The space–time regularity of pairings is not a result of numerical periodicity like in ''temporal'' simulations. It can be explained by a feedback process, generated by pairings themselves, responsible for the re-initiation of new vortex roll-up.[26,25] The feedback formula[39,7] describes how the pressure perturbation generated by vortex merging will propagate upstream and force new vortex pairings. In a low speed jet, this formula becomes[7]

$$\frac{f_iD}{V_{zc}}z_i=2\,; \tag{5}$$

$f_i=f_0/2^i$ and z_i are the frequency and the location of the *i-th* pairing, V_{zc} is the convection velocity. For the first merging location ($i=1$), the feedback formula gives $z_1=2V_{zc}/f_1=2\cdot 0.48/0.31=3.1$, a value reasonably close to that found in our visualizations $z_1\approx 3.6$.

C. Secondary stream-wise structures

At the relatively high Reynolds number considered in this section, the linear axisymmetric mode is completely destroyed by non linear effects. The subsequent frames of the flow evolution (Fig. 11) show that pairs of counter-rotating stream-wise vorticity (ω_z) filaments form in the braid region between two consecutive vortex rings. Recent experimental studies[11] and ''temporal'' direct numerical simulations[20,21] offer a complete picture of the generation and evolution of such structures in constant-density jets.

Our simulations are in very good qualitative agreement with these previous studies. The vortex rings become more distorted as they travel downstream and are subjected to azimuthal perturbations. These perturbations are amplified in the vortex sheet connecting two vortex rings and lead to the onset of stream-wise vortex filaments.[11] The space–time growth of the stream-wise filaments can be observed in Fig. 11. The stream-wise vorticity is stronger downstream of the vortex ring [Fig. 11, frame (a)], as the inviscid simulations of Martin and Meiburg[19] showed. The vortex rings remain compact and the filament growth is inhibited by vortex pairing [Fig. 11, frames (b) and (c)], a process also observed in mixing layers.[40] This stage corresponds to a linear growth of the energy content in the azimuthal velocity (Ev_θ) and the stream-wise vorticity ($E\omega_z$) (Fig. 7, $t>60$). Between $t=60$ and $t=84$, the values of $(Ev_\theta),(E\omega_z),(E\omega_r)$ are nearly constant, marking the saturation of the secondary instability. It should be also noted that the peak of stream-wise vorticity is about 20% of the peak of azimuthal vorticity and in Fig. 11 the iso-surface levels were chosen accordingly. In plane mixing layers, the measured ratio between the peaks of the stream-wise and span-wise vorticity varies between 7%[41] and 30%.[42]

The spatial distribution of the stream–wise vorticity is shown in Fig. 12 for $t=66.81$ [corresponding to frame (c) in Fig. 11]. The longitudinal cut passes through the jet axis and the core of a negative filament and the cross-stream cuts are chosen in the region of the maximum growth of the stream-wise filaments. The filaments originate from the upper (low speed) periphery of the upstream ring (cut a), extend through the braid region (cut b) and bend towards the lower (high speed) periphery of the downstream ring (cut c). New filaments start from troughs of the downstream distorted ring, which loses its coherence and breaks into lobes (cut d). In the core of vortex rings we can also observe the presence of stream-wise vorticity of opposite sign to the stream-wise vorticity on the exterior of the rings. The stream-wise structures in the ring core region are more circular than those in the braid region which are elongated in the radial direction.

These features agree with direct simulations of round jets evolving in time.[20,21] Temporal simulations show that the number of pairs of stream-wise filaments is determined by the imposed initial azimuthal perturbation. There is, so far, no evidence of a ''preferred'' azimuthal mode. This is confirmed by Cohen and Wygnanski[43] who show that resonant

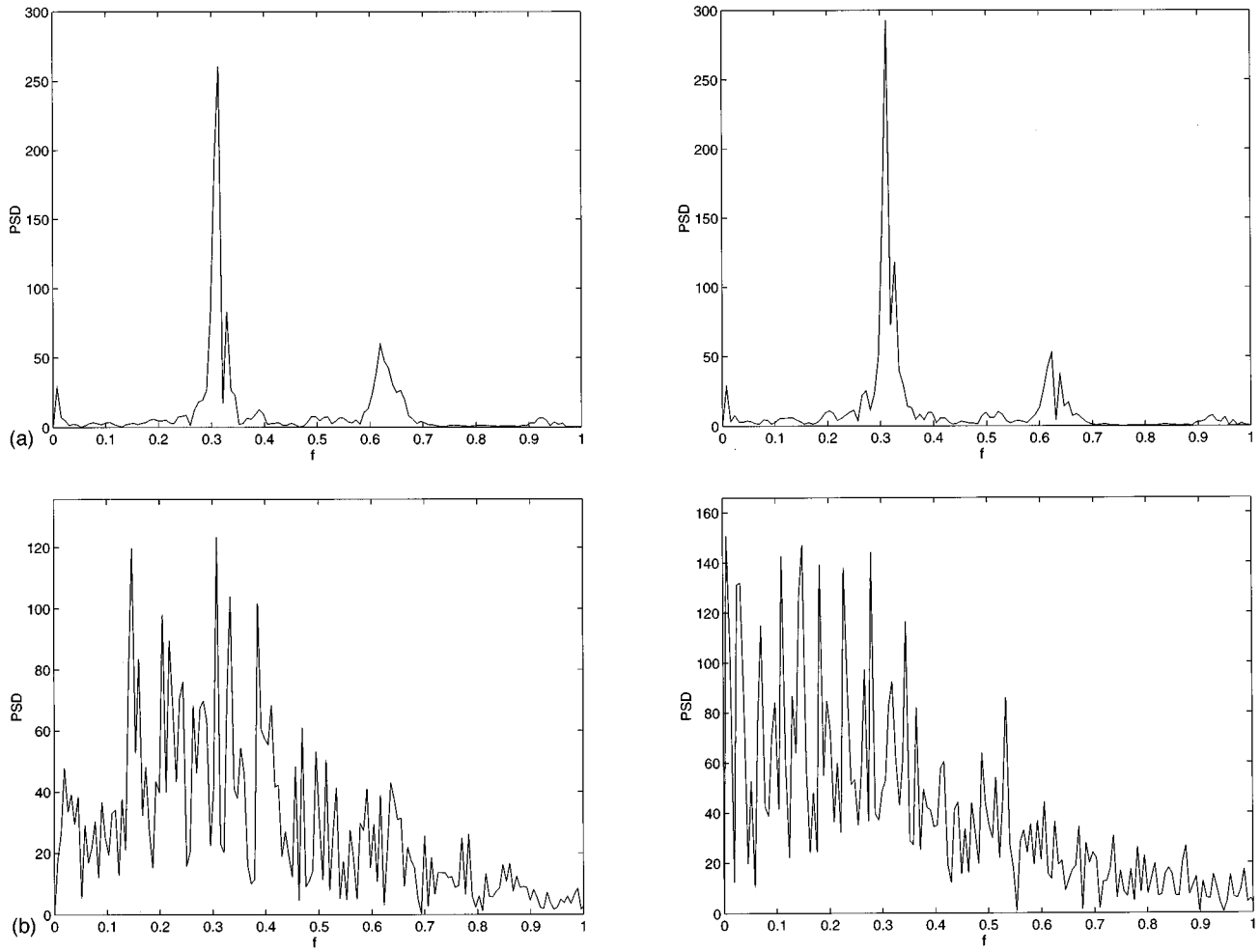

FIG. 9. $Re=500$. Spectra of the axial velocity at two different spatial locations (left) $x=y=0$, $z=2.95$ and (right) $x=y=0$, $z=4.045$. The signal in the time interval (a) $5<t<110$; (b) $100<t<260$. The vertical axis is linear and it has arbitrary units.

interactions of different azimuthal modes may generate modes with new azimuthal wave-number. Liepmann and Gharib[11] reported that the number of stream-wise structures increases with the Reynolds number; for a Reynolds number of 3000 a mode 6 was observed. In our unforced simulations, we observed a coherent azimuthal mode 4, which is probably triggered by the azimuthal distribution of the spectral elements. Further numerical tests using a refined computational domain in the azimuthal direction (grid 2 from Fig. 4) showed the same distribution of the pairs of stream-wise filaments, but their azimuthal symmetry was more rapidly broken. We can conclude that the numerical perturbation introduced at the spectral elements interfaces is a small amplitude, broadband excitation and, consequently, it can trigger only a ''natural'' mode.[44] In this latter simulation, the number of pairs of filaments does not correspond to the number of spectral elements in the azimuthal direction and the observed mode 4 is thus one of the possible unstable modes.[43]

D. Vortex rings reconnection and vortex breakup

After $t=80$ a new growth of the energy content in the azimuthal and radial vorticity components is observed in Fig. 7 indicating that the build up of the secondary stream-wise structures has finished. The dominance of the stream-wise structures downstream of 4 diameters is obvious in Fig. 11, frame (c). The stream-wise filaments are stretched by the high field strain and are pulled outward from the jet axis by the moving primary structures. Downstream of the potential core, they become strong enough to dominate the flow field [frame (d)]. A viscous diffusion process, identical to that acting on the vortex rings, is responsible for the growth of the stream-wise structures as they are convected downstream. The azimuthal symmetry of the stream-wise filaments distribution, observed in the previous frames, is lost. The vortex rings, continuously generated at the inflow boundary, become distorted at locations closer and closer to the nozzle.

The flow rapidly becomes too complex to allow a detailed description of the development of all its features. The broadband character of the spectrum of the simulated velocity signal in Fig. 9b indicates that the flow is already chaotic. Nevertheless, a last stage, involving large coherent structures, could be observed before the transition to chaos: it is the vortex reconnection between tilted rings, shown in Fig. 13 in terms of iso-surface of vorticity magnitude and selected

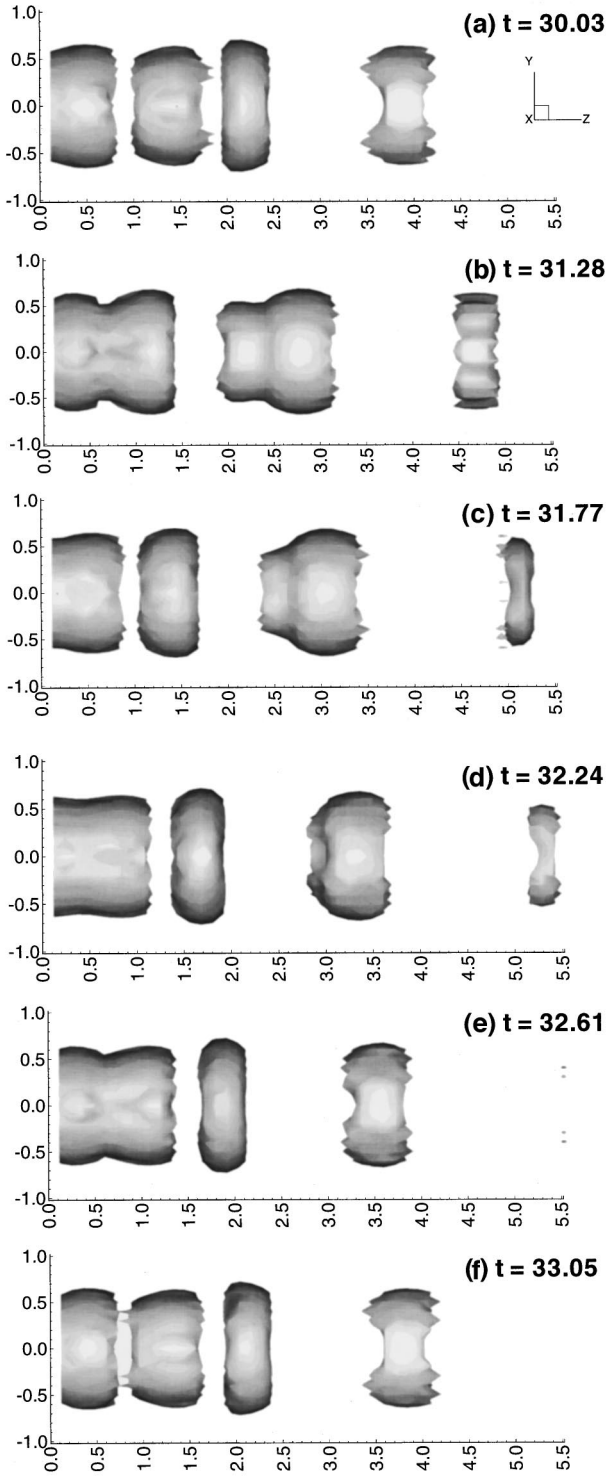

FIG. 10. $Re=500$. Vortex pairing. Instantaneous surfaces of the constant vorticity magnitude at a threshold of 35% of the maximum value.

vortex lines. It should be remarked that the correspondence of the formerly observed structures (rings and filaments) with concentrations of different components of the vorticity field (ω_θ and ω_z) is no longer valid. Vortex lines starting near the ''debris'' of vortex rings have large (spiral) incursions in the stream-wise direction, indicating that the topology of the vorticity field has changed as a result of reconnection. Before reconnection (figure not shown), the same vortex lines were circular in the vortex rings cores and presented loop deformations wrapping around the corresponding undulating rings (a similar picture is presented in Ref. 28, Fig. 7).

Based upon successive visualizations of the nonstationary field, we can speculate that the reconnection mechanism is initiated by the entrapment of the stream-wise filaments during the pairing process. Figure 14 shows the evolution of the fusion stage of the pairing process. Before the saturation of the 3D secondary instability, when the filaments are weak, the vortex ring fusion is axisymmetric and the filaments are destroyed by pairing ($t=77.16$). At later times, the stream-wise filaments structures are strong enough to persist after the pairing ($t=99.5$). The breaking of the azimuthal symmetry of the filaments distribution induces an obvious tilting of the rings before pairing ($t=120.48$). Once the tilting is produced, the induction mechanism presented by Broze and Hussain[45] (see their Figure 13) explains its amplification and the entanglement of the vortex rings. A cut-and-connected process (see Figure 15 from Ref. 44), during which two adjoining vortex structures are cross-linked, will lead to the reconnection between the partially paired rings and a newly generated and incompletely formed ring near the nozzle. The resulting spatial configuration of the vorticity field (presented in Fig. 13) has the aspect of a large helical-like structure, and could explain the ''non deterministic'' switch from the two fundamental modes ($m=0$ and $m=1$) observed in some experiments at a fixed high Reynolds number.[46]

Vortex rings, tilting and entanglement were already observed in ''temporal'' simulations of low speed compressible jets (in Ref. 47, p. 116) and in experiments.[45] The source of the initial tilting near the nozzle is not clearly explained in either reference. Broze and Hussain[45] supposed that the feedback introduced in the jet flow after the pairing will favor the upstream propagation of the azimuthal perturbations which can compete with the axisymmetrically forced disturbances. In our simulations, the entanglement and the reconnection occur between strongly deformed rings at the points of the connection with the filaments. Hussain[44] observed in plane mixing layers that, as the ribs (equivalent to filaments in our case) are wrapped around the rolls ($\equiv$ rings), vortex lines are turned and aligned with the flow, causing large local coherent helicity. The local helicity could be responsible for the initial tilting of the rings. In the same time, the points of interaction between rolls and ribs are evidenced in plane mixing layers as the sites of strongest mixing and three-dimensional turbulence.[42,48] The small scales transition is beyond the scope of the present paper and needs further investigations.

V. HELICAL MODES AT LOW REYNOLDS NUMBERS

A. Primary instability onset

Keeping the same resolution as in the previous section it was possible to observe the unstable jet at Reynolds numbers exceeding only slightly the value of 300. At this Reynolds number the helical modes dominate the instability. The basic difficulty in investigating the instability development for only slightly supercritical Reynolds numbers is the necessity

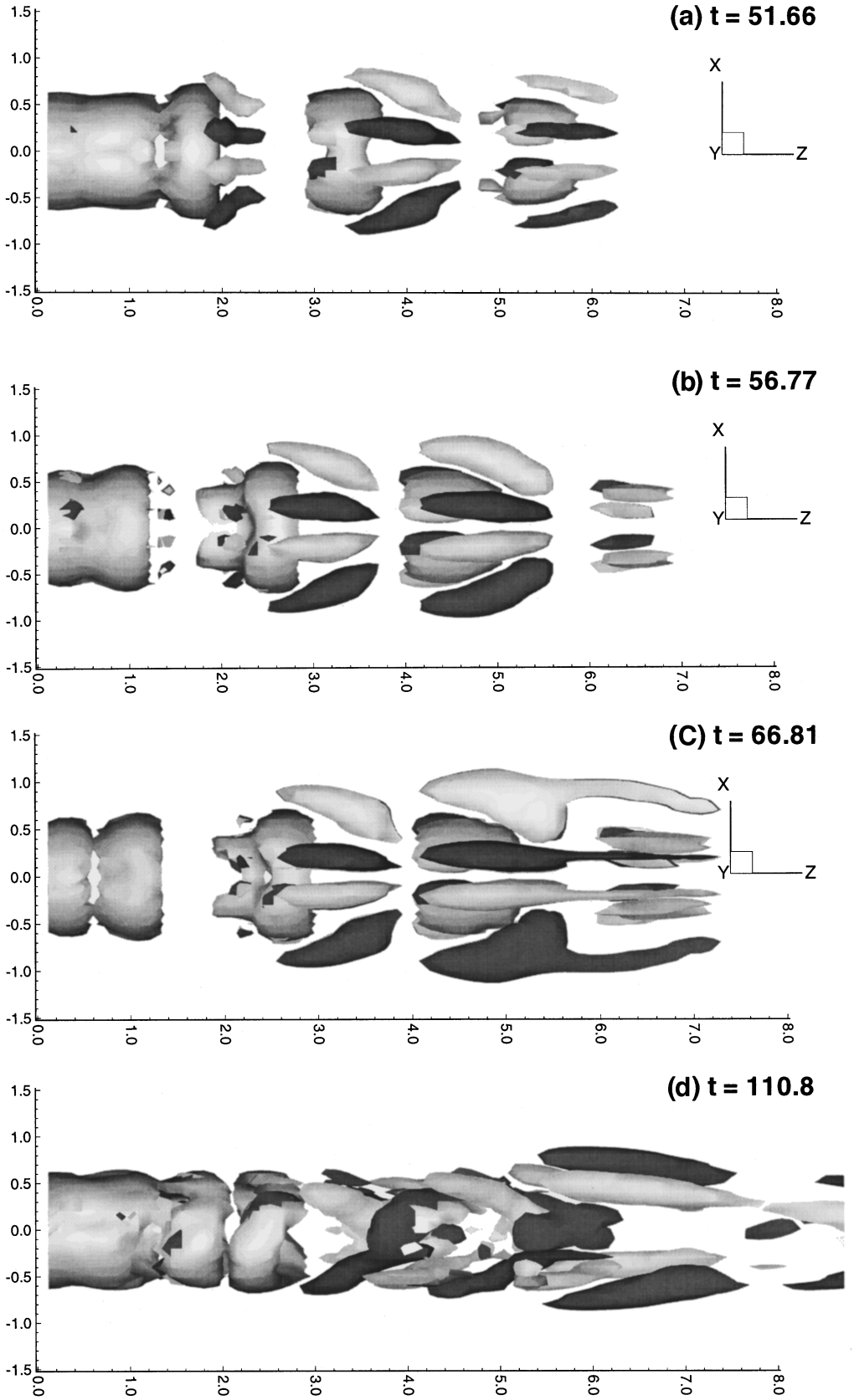

FIG. 11. $Re=500$. Stream–wise vortex filaments. Instantaneous surfaces of constant azimuthal vorticity (grey), stream-wise vorticity (white for positive and black for negative) at a threshold corresponding to 35% of the respective maxima and minima.

to simulate very long transients. For this reason the spatial discretization accuracy was decreased to 7 collocation points per spatial direction for most simulations. This more than halves the number of nodes and increases the time step resulting from the stability requirements by a factor of 2 as compared to the simulation in Section IV (see also the numerical tests in Section II B). Moreover, the increased numerical noise allowed to lower the Reynolds number to 225.

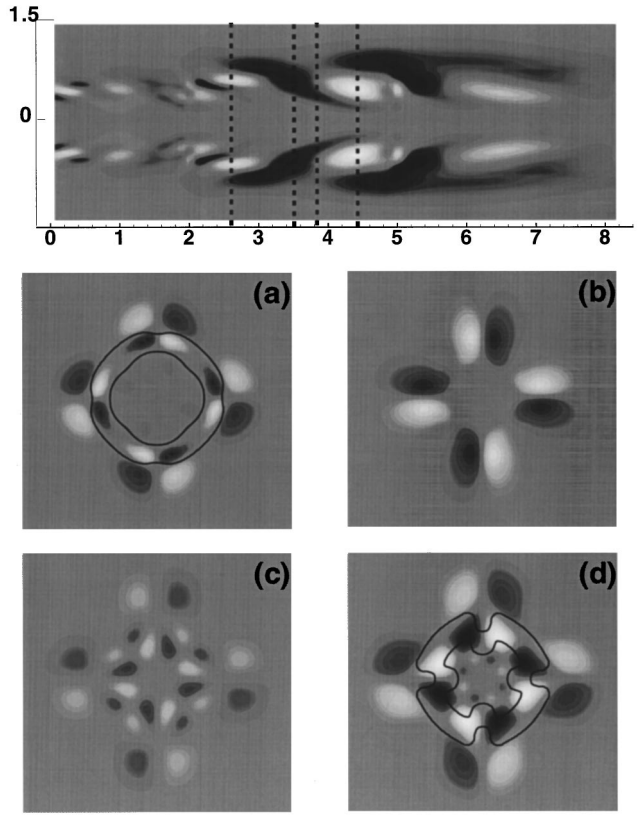

FIG. 12. $Re=500$, $t=66.81$. Spatial distribution of the stream-wise vorticity (black for negative and white for positive). A longitudinal cut through the jet axis and the core of a negative filament ($\theta=15^{o}$). Transverse cuts at $z=2.8$ (a), $z=3.5$ (b), $z=3.93$ (c) and $z=4.5$ (d). The lines in (a) and (d) represent contours of the azimuthal vorticity at 35% of the maximum and mark the vortex rings.

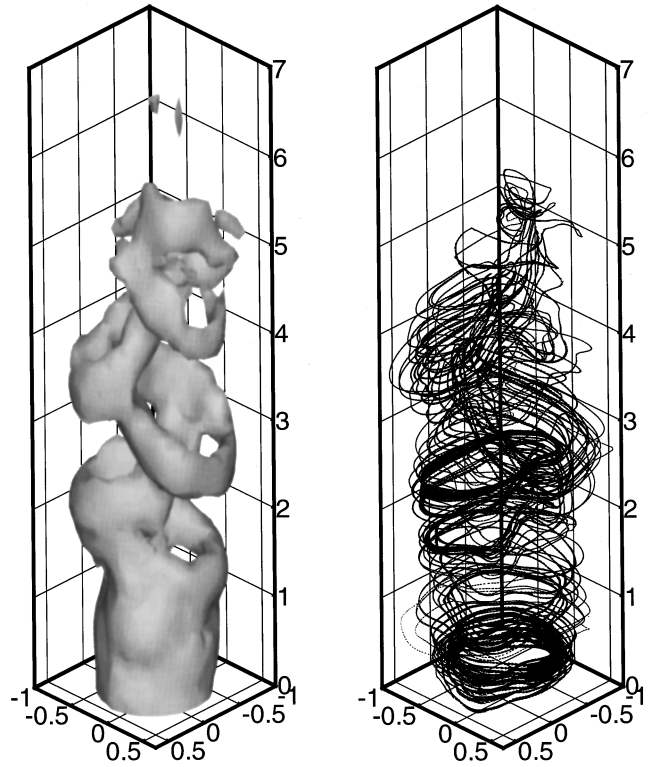

FIG. 13. $Re=500$, $t=131.4$. Vortex rings reconnection in helical structures. An instantaneous surface of constant vorticity magnitude at a threshold of 35% of the maximum value and selected vortex lines.

As far as the capture of the smallest structures of the flow is concerned, the decrease of the used resolution is compatible with the increase of the size of the small structures due to the decrease of the Reynolds number from 500 to 225.

The instability threshold was determined by studying the instability dampening or amplification of an already unsteady flow. For this purpose, a slightly perturbed unsteady flow was obtained by setting a rather significantly sub-critical Reynolds number and letting the instability fluctuations obtained at a significantly supercritical Reynolds number settle to a level of less than 10^{-3} of the inflow velocity value. Then the Reynolds number was progressively increased until amplification became perceptible. This allowed us to obtain rather rapidly an acceptable approximation of a slightly perturbed basic flow at nearly critical Reynolds numbers suitable for the investigation of the instability onset and development.

A perturbation of such a low level can very well be considered linear. At Reynolds numbers slightly exceeding $Re=200$ the instability was found to be characterized by oscillations with a non-dimensional frequency of 0.169, i.e. roughly half the *preferred* frequency found at $Re=500$. The amplification rate was found to be very weak and the low level could be maintained for sufficiently many instability oscillations to determine the instability threshold without difficulty. The latter was found to be $Re_{crit}\approx 220$ for the chosen discretization accuracy. The oscillating character of the instability shows that it is of the Hopf type.

B. Primary instability development and structure

The obtained instability was allowed to develop to see the nature of the attractor that is reached. In spite of a rather detailed investigation of very nearly critical Reynolds numbers, a limit cycle could not be observed. Instead, a limit torus dynamics has been evidenced (Fig. 15) even very close to the instability threshold. Note the perfect Hopf-like instability onset in the early stages of the instability development which is ending, however, in a quasiperiodic final state. Note also the level of oscillation amplitude of only 0.04 of the inflow velocity which is obtained due to the proximity of the instability threshold at $(Re-Re_{crit.})/Re_{crit.}=2\%$.

To better understand the reasons of such a behavior, we analyzed the flow by extracting the Fourier components of the instability (see Refs. 30, 49) by the method described in Ref. 50. The Fourier analysis was carried out over the time corresponding to one oscillation. The angular frequency of the linear unstable mode is strictly the same throughout the flow. Close to the instability threshold, the amplification rate is so small that, in the linear regime, the amplification over one oscillation period can be neglected and a standard Fourier integration over one period can be used. In the saturation regime, more than 40 oscillations per beating have been found (Fig. 15), which allows us, once again, to consider the modulation negligible during one single oscillation.

The flow field decomposition has been added to the original code and yields the Fourier components of all veloc-

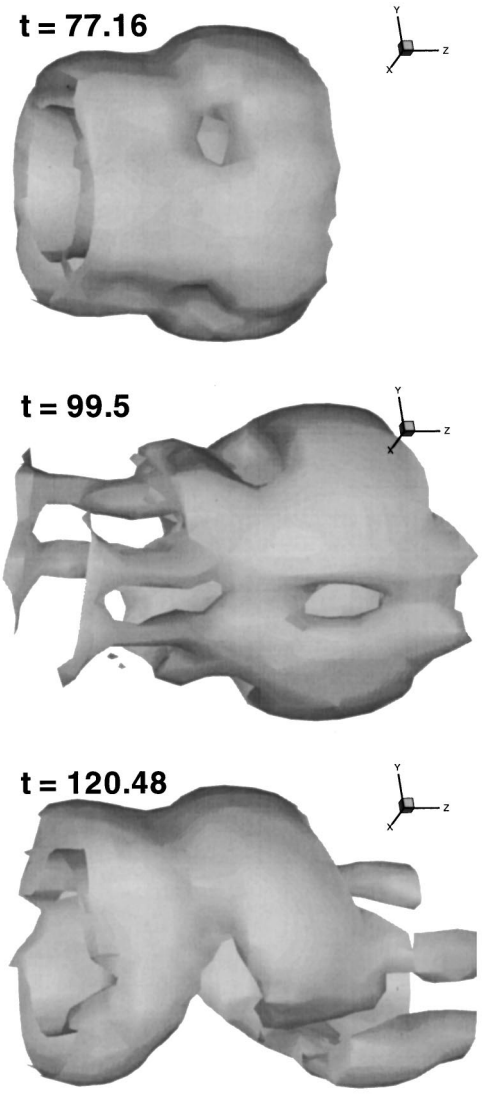

FIG. 14. $Re=500$. Fusion stage of the vortex ring pairing for different times. Instantaneous surface of constant vorticity magnitude at a threshold of 35% of the maximum value. The visualized domain extent is $1.5<z<3.5$.

ity components and of the pressure at each node of the discretization. Considering that at each node of the computational domain the signals have a periodicity T in time t, the velocity and pressure fields (v_r, v_θ, v_z, p) can be expressed as a Fourier series:

$$\mathbf{v}(r,\theta,z,t)=\sum_{n=-\infty}^{+\infty}\mathbf{c}_n(r,\theta,z)e^{in\omega t}, \tag{6}$$

where $\omega=2\pi/T$ and the coefficients c_n have been computed as

$$\mathbf{c}_n(r,\theta,z)=\frac{1}{T}\int_0^T\mathbf{v}(r,\theta,z,t)dt. \tag{7}$$

Due to the original axisymmetry of the flow, axisymmetry breaking can be expected to occur via an onset of harmonics in the azimuthal direction θ. The Fourier modes obtained above have therefore been further decomposed along the azimuthal direction:

$$\mathbf{c}_n(r,\theta,z)=\sum_{m=-\infty}^{+\infty}\mathbf{c}_{n,m}(r,z)e^{-im\theta}, \tag{8}$$

with the coefficients $c_{n,m}$ calculated as

$$\mathbf{c}_{n,m}(r,z)=\frac{1}{2\pi}\int_0^{2\pi}\mathbf{c}_n(r,\theta,z)e^{im\theta}d\theta. \tag{9}$$

The final decomposition of the flow field can be expressed as

$$\mathbf{v}(r,\theta,z,t)=\sum_{n,m=+\infty}^{-\infty}\mathbf{c}_{n,m}(r,z)e^{i(n\omega t-m\theta)}. \tag{10}$$

The mode $n=0,m=0$ contains the basic axisymmetric flow field and, close to the instability threshold, only a small non linear correction. The most relevant information about the instability is provided by the fundamental $n=1$, that can be assumed to be practically identical to the linear mode so close to the instability threshold.

The fundamental component of the signals (determined by letting $n=1$) accurately describes the linear unstable mode and its analysis shows that it can be identified as a superposition of two counter-rotating helical modes ($m=1$ and $m=-1$) quantified by the coefficients $c_{1,1}$ and $c_{1,-1}$. The ''raw'' fundamental fluctuating flow field, representing practically the total fluctuation field, and the individual modes $c_{1,1}$ and $c_{1,-1}$ are shown in Fig. 16 in terms of iso-surfaces of stream-wise vorticity. The growth of a vortex helix corresponds to the region of negative stream-wise vorticity in Fig 16. Owing to the helical symmetry, the stream-wise vorticity in the braid (this time, the region between two loops of the helix) has an opposite sign and appears to spiral around the concentrated negative region of stream-wise vorticity. Note that the two modes have different magnitudes. The helical structures are similar to those found by Martin and Meiburg[51] in their ''temporal'' vortex filaments simulations. They also reported that for a ratio of $R/\Theta=22.6$ the (forced) single helix is stable and avoids azimuthal instability. This is also the case in our unforced simulations ($R/\Theta\approx 20$): no concentrated stream-wise braid vortices were observed.

The individual modes $c_{1,1}$ and $c_{1,-1}$ can be identified as the helical modes predicted by the linear stability theory.[13,16,4] If we neglect the stream-wise dependence of the mode envelope and wavelength due to the non parallel character of the basic flow, it is possible to write, approximately,

$$\mathbf{c}_{n,m}(r,z)=\tilde{\mathbf{c}}_{n,m}(r)e^{-ikz}, \tag{11}$$

where $k=2\pi/\lambda_z$ is the stream-wise wavenumber, and the decomposition of the fluctuating flow field can be expressed as

$$\mathbf{v}'(r,\theta,z,t)=\sum_{m=\pm 1}\tilde{\mathbf{c}}_{1,m}(r)e^{i(\omega t-m\theta-kz)}+\text{c.c.} \tag{12}$$

The coefficients $\tilde{\mathbf{c}}_{1,m}(r)$ have been fitted to the calculated discrete coefficients at a fixed point chosen $7.5D$ downstream of the nozzle. The resulting ''parallel'' fluctuating field is represented in Fig. 17. It offers a qualitatively good description of the ''real'' fluctuating flow field in Fig. 16. If

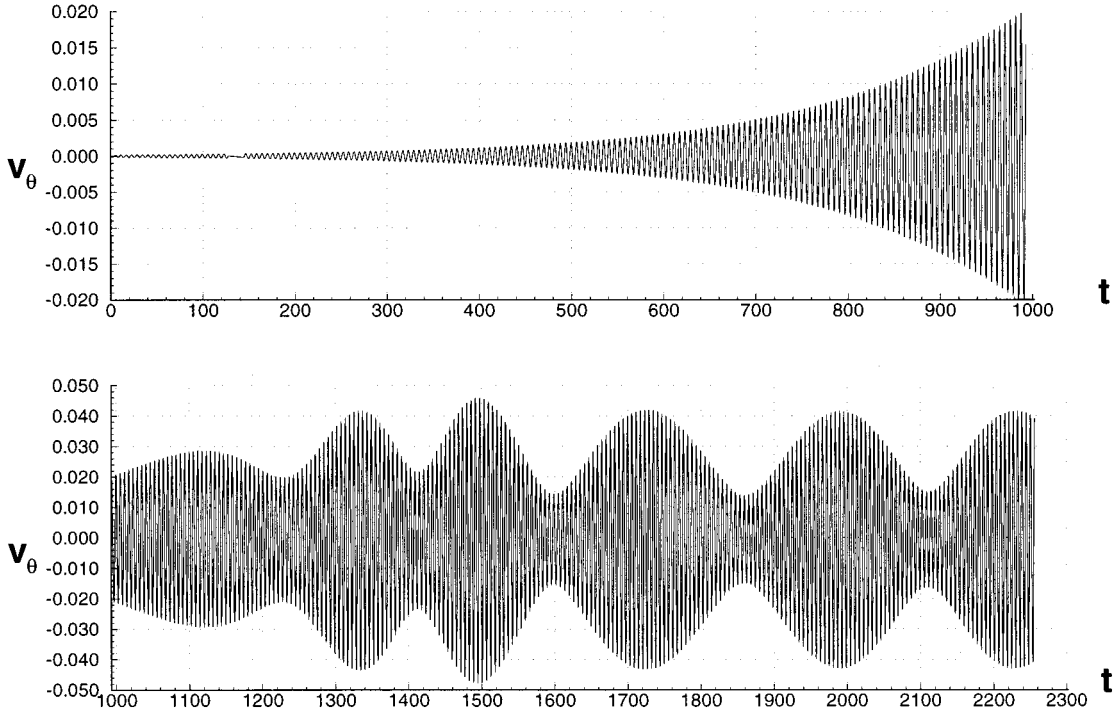

FIG. 15. $Re=225$. The azimuthal velocity (v_θ) signal at a location in the mixing layer ($x=0.507$, $y=0$, $z=2$). Signal in the linear regime (above) and in the asymptotic state (below). The initial condition is the stationary flow field calculated for $Re=220$.

both $m=1$ and $m=-1$ modes were of similar strength, the pattern would be an alternating series of oppositely shaded surfaces, disposed in sinusoids or axisymmetric shapes depending on the angle of visualization (Fig. 18). This last structure has been reported by Yoda *et al.*[52] in the self-similar region of a round jet.

The linear theory shows that both modes are eigensolutions of the linear eigenvalue problem associated to the same unstable eigenvalue. The phase difference and the relative magnitude of the two counter-rotating modes in the linear regime thus result from the initial conditions. This is easily confirmed by studying the fluctuating field structure for varying initial conditions using the flow field decomposition (10). In our first simulation both modes were represented since the very beginning. We then created a new initial condition containing only the first helical mode by keeping only the terms $c_{0,0}$, representing approximately the basic flow, and $c_{1,1}$, representing only the counter-rotating helical initial perturbation, in the sum (10). The obtained velocity oscillation signal in the linear regime and in the asymptotic state appeared to be identical to that in Fig. 15. The presence of modes $c_{1,\pm1}$ was monitored by computing, for each analyzed period T,

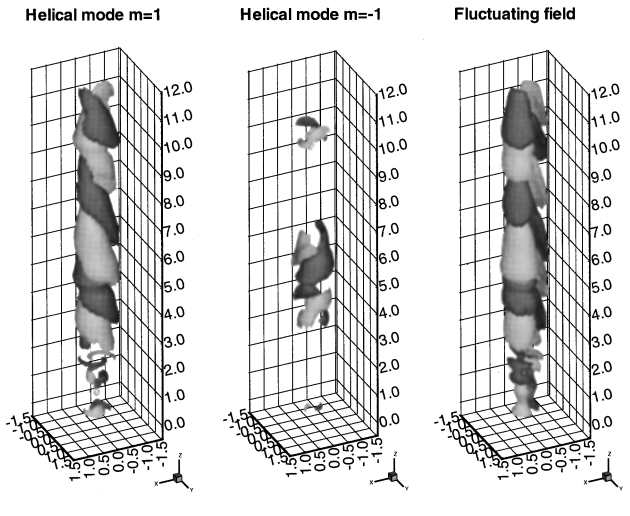

FIG. 16. $Re=225$. Decomposition of the fluctuating field in helical modes. From left to right: mode $m=1$, mode $m=-1$ and the fluctuating field. Surfaces of constant stream-wise vorticity (white for positive and black for negative) at a threshold corresponding to 35% of the respective maxima and minima.

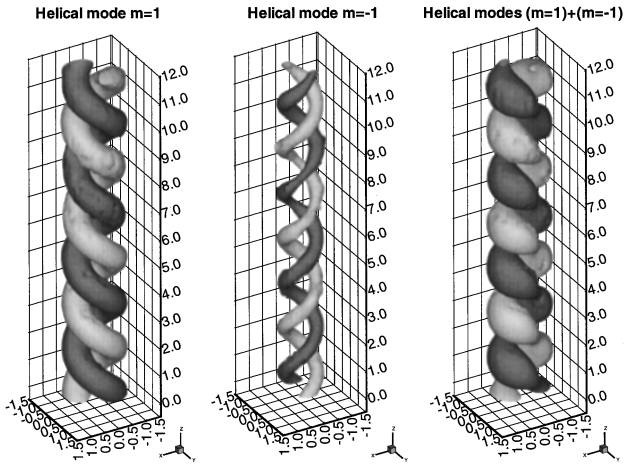

FIG. 17. Analytical ''parallel'' model of the helical modes $m=\pm1$ and the resulting flow pattern from their superposition. Surfaces of constant stream-wise vorticity (grey for positive and black for negative); the same threshold is used in the three frames.

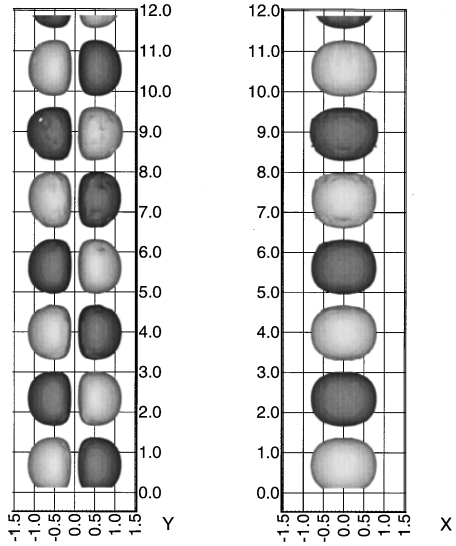

FIG. 18. Flow pattern obtained by superposition of the two theoretical helical modes $m=\pm 1$ of the same strength. Surfaces of constant stream-wise vorticity (grey for positive and black for negative).

the three components of the mean kinetic energy of the helical modes, which can be evaluated in the spectral space as

$$K_m(\mathbf{v}) = \int_\Omega |c_{1,m}|^2 d\Omega, \tag{13}$$

where Ω is the computational domain, $m=\pm 1$, and $\mathbf{v}=(v_r, v_\theta, v_z)$. Applying this analysis for different periods considered at different times of the simulation, we can draw the time evolution of the kinetic energy of the two helical modes. The two calculation cases display similar evolutions, as shown in Fig. 19.

The initial helical mode $m=1$ grows linearly and reaches a local maximum level ($t\approx 850$). The subsequent decay of its energy is related to the emergence of the counter-rotative

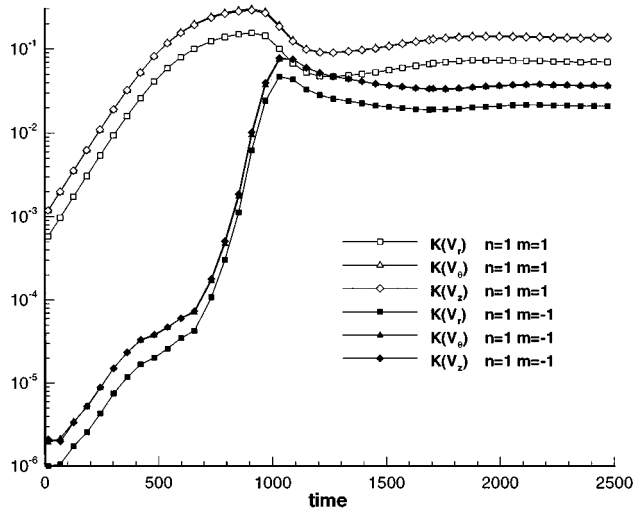

FIG. 19. $Re=225$. Time evolution of the components of the kinetic energy evaluated in the spectral space. The operator (K) is given by eq. (13). Simulation starting from an initial condition containing only the first helical mode $m=1$.

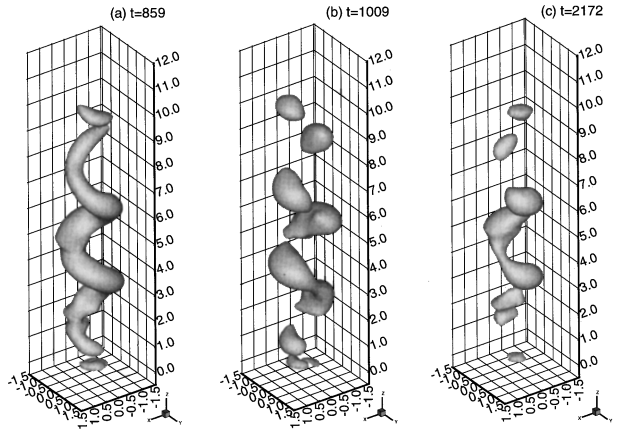

FIG. 20. $Re=225$. Surface of the constant pressure fluctuation. The same threshold is used in the three frames and it corresponds to $p=1/3p_{min}$ calculated for $t=2172$. The initial condition containing only the first helical mode $m=1$. Different times corresponding to those shown in Fig. 19.

helical counterpart $m=-1$. The growth of the latter passes also through a maximum ($t\approx 1000$). Finally the modes settle to a constant level which is not the same for $m=1$ and $m=-1$. These two observed modes correspond to the same eigenvalue, i.e., they have the same oscillation frequency in the linear regime. The same final levels have been obtained in this simulation and in the first one where both modes were present in the initial condition. Iso-surfaces of low pressure calculated in the fluctuating field at the three mentioned instants are represented in Fig. 20. We can conclude that the observed beatings are explained by a slight frequency difference between the modes $m=1$ and $m=-1$ resulting from non-linear effects in the saturated state.

VI. FINAL DISCUSSION AND CONCLUSIONS

Much of the literature concerning the near-field dynamics of round jet flows mostly emphasizes the growth and evolution of axisymmetric disturbances. The linear inviscid analysis of Batchelor and Gill[12] and Mattingly and Chang,[13] however, pointed out that the first helical mode has amplification characteristics identical to those of the axisymmetric mode. The viscous linear theory of Morris[16] further suggested that the selection of the axisymmetric or the helical mode is very sensitive to initial perturbations like the local unsteady pressure field at the lip of the jet. These speculations were confirmed by the experiments of Corke *et al.*[46] who indicated that the observed switching between these two fundamental modes is the result of the response of the jet to randomly arriving axisymmetric or non-axisymmetric disturbances at the jet lip. They also showed that the axisymmetric and the helical modes do not exist neither at the same time nor in the same place. Most of analytical and experimental studies suggest that the ratio of the nozzle diameter (D) to the initial momentum thickness (Θ_0) is the parameter indicating which of the axisymmetric or the helical mode is the most amplified in the near field of the round jet. As the shear layer grows (i.e., D/Θ_0 diminishes), the helical mode becomes dominant over the axisymmetric mode.[17]

In the present study, for a ''top-hat'' inflow velocity profile, we showed that the Reynolds ($Re = V_{z0}D/\nu$) number is the parameter selecting the most amplified unstable mode, when it varies between 200 and 500. Helical modes are selected at lower Reynolds numbers and the axisymmetric mode at higher Reynolds numbers, as expected from the predictions of the viscous linear stability theory analysis[16,35] and from experimental observations.[5] The quantitative agreement with the local parallel theory obtained for mean velocity profiles close to the nozzle confirm that the zone extending a few diameters downstream of the nozzle is most important for the onset of the instability. A global effect of this zone results in a definite mode and frequency selection.

Direct numerical simulations of unforced, spatially evolving round jets offered an ideal framework for this study; random initial perturbations occurring in experiments are avoided and information concerning the global effect of the downstream structures on the instability onset is available, in contrast to frequently used ''temporal'' simulations. In addition, unlike experiments where a variation in the jet exit velocity yields a different initial momentum thickness, in our numerical simulations the parameter R/Θ_0 of the inflow velocity profile is fixed by the finite discretization and the influence of the Reynolds number, as a single parameter, can be studied.

The investigation allowed us to identify the large structures dominating the unstable jet. For a Reynolds number of 500 the spontaneous destabilization of an axisymmetric flow was investigated, providing results similar to those already published for larger Reynolds numbers. In accordance with theoretical predictions, the onset of instability was found to be governed by the inviscid, axisymmetric Kelvin–Helmholtz mechanism. The vorticity concentrates into ring vortices while the braid regions become depleted. The shear layer grows by viscous diffusion and vortex ring merging. Our simulation allowed, however, to follow all the subsequent stages of transition to a chaotic state. After completion of the vortex pairing, formation of secondary pairs of counter-rotating stream-wise filaments in the braid region could be obtained without any artificial perturbations. The obtained quantitative characteristics of this stage of jet development, such as the Strouhal number of the vortex ring shedding, the ''preferred'' Strouhal number and the downstream distance of vortex merging, are in good agreement with previous experimental and analytical results. The form of the stream-wise structures agrees with that found in direct simulations of round jets evolving in time. In the last stage of simulation, the spatial evolution of these structures could be visualized and the role of the stream-wise filaments in vortex ring re-connections leading to the final vortex breakup could be evidenced.

The coherent structures we identified in the flow field are different for low supercritical Reynolds numbers in the immediate neighborhood of the instability threshold. The primary instability is then characterized by symmetry breaking, resulting from the presence of two equally amplified counter-rotating helical modes $m=1$ and $m=-1$. This change in the selection of the most unstable mode with the Reynolds number can explain the experimental observations of Crow and Champagne[5] reporting the shift of the jet shape from a helix to a train of axisymmetric waves, when the Reynolds number is increased from 100 to 1000. A Fourier mode analysis of the fluctuating field allowed us to clearly identify these helical modes as responsible for the observed flow pattern. The relative strength of these two modes is determined throughout the whole linear regime by initial conditions. In the asymptotic state both modes have well defined levels largely independent of the initial conditions. Non linear effects then determine the frequency shifts with respect to the linear frequency. This results in beatings appearing in the velocity signals. This feature might be characteristic for all axisymmetric flows and is to be related to the degeneracy of the spectrum of the linear Navier–Stokes operator giving rise to two different unstable modes. Axisymmetry breaking thus leads directly to a limit torus dynamics right at the primary bifurcation. An interval of Reynolds numbers was found to be characterized by such dynamics but, according to our results, the chaotic stage then appears to set in quite early.

ACKNOWLEDGMENTS

This work was funded by l'Institut National de l'Environnement Industriel et des Risques (I.N.E.R.I.S.). We are grateful for their support. Nekton is a registered trademark of Nektronics, Inc. and the Massachusetts Institute of Technology. ©1991 by creare.x, Inc., Hanover, New Hampshire.

[1] H. A. Becker and T. A. Massaro, ''Vortex evolution in a round jet,'' J. Fluid Mech. **31**, 435 (1968).
[2] A. Viilu, ''An experimental determination of the minimum Reynolds number for instability in a free jet,'' J. Appl. Mech. **29**, 506 (1962).
[3] A. J. Reynolds,''Observation of a liquid-into-liquid jet,'' J. Fluid Mech. **14**, 552 (1962).
[4] J. C. Mollendorf and B. Gebhart, ''An experimental and numerical study of the viscous stability of a round laminar vertical jet with and without buoyancy for symmetric and asymmetric disturbance,'' J. Fluid Mech. **61**, 367 (1973).
[5] S. C. Crow and F. H. Champagne, ''Orderly structure in jet turbulence,'' J. Fluid Mech. **48**, 547 (1971).
[6] P. Huerre and P. A. Monkewitz, ''Absolute and convective instabilities in free shear flows,'' J. Fluid Mech. **159**, 151 (1985).
[7] G. Gutmark and C. M. Ho, ''Preferred modes and the spreading rates of jets,'' Phys. Fluids **26**, 2932 (1983).
[8] C. M. Ho and P. Huerre, ''Perturbed free shear layers,'' Annu. Rev. Fluid Mech. **16**, 365 (1984).
[9] A. J. Yule, ''Large structures in the mixing layer of a round jet,'' J. Fluid Mech. **89**, 413 (1978).
[10] C. M. Ho and L. S. Huang, ''Subharmonics and vortex merging in mixing layers,'' J. Fluid Mech. **119**, 443 (1982).
[11] D. Liepmann and M. Gharib, ''The role of streamwise vorticity in the near-field entrainment of round jets,''J. Fluid Mech. **245,** 643 (1992).
[12] G. K. Batchelor and A. E. Gill, ''Analysis of the stability of axisymmetric jets,'' J. Fluid Mech. **14**, 529 (1962).
[13] G. E. Mattingly and C. C. Chang, ''Unstable waves on an axisymmetric jet column,'' J. Fluid Mech. **65**, 541 (1974).
[14] P. Plaschko, ''Helical instabilities of slowly divergent jets,'' J. Fluid Mech. **92**, 209 (1979).
[15] A. Michalke and G. Hermann, ''On the inviscid instability of a circular jet with external flow,'' J. Fluid Mech. **21**, 159 (1984).
[16] P. J. Morris ''The spatial viscous instability of axisymmetric jets,'' J. Fluid Mech. **77**, 511 (1976).
[17] J. Cohen and I. Wygnanski, ''The evolution of instabilities in the axisymmetric jet. Part 1. The linear growth of disturbances near the nozzle,'' J. Fluid Mech. **176**, 191 (1987).
[18] J. Dušek, Ph. Fraunié, and P. Le Gal, ''Local analysis on the onset of

instability in shear flows,'' Phys. Fluids **6**, 172 (1994).
[19]J. E. Martin and E. Meiburg, ''Numerical investigation of the three-dimensionally evolving jets subject to axisymmetric and azimuthal perturbations,'' J. Fluid Mech. **230**, 271 (1991).
[20]M. Abid and M. Brachet, ''Numerical characterization of the dynamics of vortex filaments in round jets,'' Phys. Fluids A **5**, 2582 (1993).
[21]P. Brancher, J. M. Chomaz, and P. Huerre, ''Direct numerical simulations of round jets: Vortex induction and side jets,'' Phys. Fluids **6**, 1768 (1994).
[22]R. Verzicco and P. Orlandi, ''Direct simulations of the transitional regime of a circular jet,'' Phys. Fluids **6**, 751 (1994).
[23]J. B. Freund, S. K. Lele, and P. Moin, ''Direct simulation of a supersonic round turbulent shear layer,'' AIAA Paper 97–0760, 1997.
[24]M. Gaster, ''A note on the relation between temporally-increasing and spatially-increasing disturbances in hydrodynamic stability,'' J. Fluid Mech. **14**, 222 (1962).
[25]R. W. Davis and E. F. Moore, ''A numerical study of vortex merging in mixing layers,'' Phys. Fluids **28**, 1626 (1985).
[26]F. F. Grinstein, E. S. Oran, and J. P. Boris, ''Direct numerical simulations of axisymmetric jets,'' AIAA J. **25**, 92 (1987).
[27]F. F. Grinstein, E. S. Oran, and A. K. M. F. Hussain, ''Simulation of the transition region of axisymmetric free jets,'' in *Proceedings of the T. S. F. 6*, Toulouse, 1987, p. 10-6-1.
[28]F. F. Grinstein, E. J. Gutmark, T. P. Parr, D. M. Hanson-Parr, and U. Obeysekare, ''Stream-wise and spanwise vortex interaction in an axisymmetric jet. A computational and experimental study,'' Phys. Fluids **8**, 1515 (1996).
[29]M. Olsson and L. Fuchs, ''Large eddy simulation of the proximal region of a spatially developing circular jet,'' Phys. Fluids **8**, 2125 (1996).
[30]J. Dušek, P. Le Gal, and Ph. Fraunié, ''A numerical and theoretical study of the first Hopf bifurcation in a cylinder wake, '' J. Fluid Mech. **264**, 59 (1994).
[31]V. Pagneux and A. Maurel,''Etude numérique d'instabilités en écoulements ouverts confinés,'' C. R. Acad. Sci. Paris **t. 319**, 617 (1994).
[32]G. P. Neitzel, C. S. Kirkconnell, and L. J. Little, ''Transient, nonaxisymmetric modes in the instability of unsteady circular Couette flow. Laboratory and numerical experiments.'' Phys. Fluids **7**, 324 (1995).
[33]J. Dušek and Ph. Fraunié, ''Validation and error estimate of a spectral element discretization of a cylinder wake,'' in *Numerical Methods in Laminar and Turbulent Flows '93*, edited by C. Taylor (Pineridge, Swansea, UK, 1993), Vol. VIII, Part 1.
[34]Ch. Dauchy, J. Dušek, and Ph. Fraunié, ''Primary and secondary instability in the wake of a cylinder with free ends,'' J. Fluid Mech. **332**, 295 (1997).
[35]A. Michalke, ''Survey on jet instability theory,'' Prog. Aerosp. Sci. **21**, 159 (1984).
[36]J. C. Buell and P. Huerre, ''Inflow/outflow boundary conditions and global dynamics of spatial mixing layers,'' Summer Program Report No. CTR–S88, 1988, p. 19.
[37]J. Jeong and F. Hussain, ''On the identification of a vortex,'' J. Fluid Mech. **285**, 69 (1995).
[38]R. S. Miller, C. K. Madnia, and P. Givi, ''Numerical simulation of non-circular jets,'' Comput. Fluids **24**, 1 (1995).
[39]J. Laufer and P. A. Monkewitz, ''On turbulent jet flows: A new perspective,'' AIAA Paper No. 80–0962, 1980.
[40]R. W. Metcalfe, S. A. Orszag, M. E. Brachet, S. Menon, and J. J. Riley, ''Secondary instability of a temporally growing mixing layer,'' J. Fluid Mech. **184**, 207 (1987).
[41]S. Tung, S. and J. Kleis, ''Initial streamwise vorticity formation in a two-stream mixing layer,'' J. Fluid Mech. **319**, 251 (1996).
[42]L. -S. Huang and C. -M. Ho, ''Small-scale transition in a plane mixing layer,'' J. Fluid Mech. **119**, 475 (1990).
[43]J. Cohen and I. Wygnanski, ''The evolution of instabilities in the axisymmetric jet. Part 2. The flow resulting from the interaction between two waves,'' J. Fluid Mech. **176**, 221 (1987).
[44]A. K. M. F. Hussain, ''Coherent structures and turbulence,'' J. Fluid Mech. **173**, 303 (1986).
[45]G. Broze and F. Hussain, ''Transition to chaos in a forced jet: Intermittency, tangent bifurcations and hysteresis,'' J. Fluid Mech. **311**, 37 (1996).
[46]T. C. Corke, F. Shakib, and H. M. Nagib, ''Mode selection and resonant phase locking in unstable axisymmetric jets,'' J. Fluid Mech. **223**, 253 (1991).
[47]M. Lesieur, *La Turbulence* (Presses Universitaires de Grenoble, Grenoble, 1994).
[48]M. M. Rogers and R. D. Moser, ''The three-dimensional evolution of a plane mixing layer: The Kelvin–Helmholtz rollup,'' J. Fluid Mech. **243**, 183 (1992).
[49]G. Carte, J. Dušek, and Ph. Fraunié, ''A spectral time discretization for flows with dominant periodicity,'' J. Comput. Phys. **120**, 171 (1995).
[50]J. Dušek, ''Spatial structure of the Bénard–von Kármán instability,'' Eur. J. Mech. B Fluids **15**, 619 (1996).
[51]J. E. Martin and E. Meiburg, ''Numerical investigation of three-dimensionally evolving jets under helical perturbations,'' J. Fluid Mech. **243**, 457 (1992).
[52]M. Yoda, L. Hesselink, and G. Mungal, ''Instantaneous three-dimensional concentration measurements in the self-similar region of a round high-Schmidt-number jet,'' J. Fluid Mech. **279**, 313 (1994).